Automated Magnetic Particle Attachment to an Atomic Force Microscope Cantilever

Thesis

Presented in Partial Fulfillment of the Requirements for

The Degree Master of Science in the

Graduate School of The Ohio State University

By

Atul Nagose, B.Tech. M.E.

* * * * *

The Ohio State University

2009

Master's Examination Committee:

Dr. Chia-Hsiang Menq, Advisor

Dr. Gary Kinzel

Approved by

_____

Advisor
Graduate Program in
Mechanical Engineering

ABSTRACT

The traditional Atomic Force Microscope (AFM) is a two-dimensional tool, which can only generate surface profile with limited depth variation. A design modification to the traditional AFM has been proposed by Jayanth et.al [1] to make it a true three-dimensional tool. The modified cantilever has a magnetic particle attached to it. These particles are attached indigenously on the commercially available cantilevers. The magnetic particle attachment process is very sensitive to vibration and requires very precise motion control avoiding any unnecessary body movement. Since conventionally it has been done manually, it imposes stringent constraints on the user performing this task. A more accurate and faster process was required to replace the existing system. This thesis develops an automated process for attaching a magnetic particle to the AFM cantilever. The new process requires very little manual involvement in the most critical steps of the process.

A setup was designed to incorporate the visual feedback from a camera attached to a microscope and actuation using a three-axis piezo stage. The image formation process was modeled relating any three-dimensional point to its corresponding location in the image captured by a Charge Coupled Device (CCD) chip. Image processing

algorithms were developed to locate the particle, micro-pipette and the AFM cantilever, also to track the particle and micro-pipette in real-time. Finally a control system was designed which would control the location of the object (micro-pipette or the particle) by actuating the piezo stage. The control system used image from only one camera, while the hysteresis in the piezo stage, which was being operated in open loop, was countered for.

The control system was tested for automating different steps in the process. It was first calibrated to extract the necessary system parameters. Its robustness was tested by performing the process under varying illumination and vibration. The process could successfully attach particles of size ranging from 25 – 70 μm under these conditions. The automated process was twice as fast as the manual process and required minimal manual involvement in the particle attachment step. Similar results were observed for other steps that were automated, specifically the particle pick-up and glue dabbing step.

Dedicated to my parents who have always supported me in all my decisions

ACKNOWLEDGEMENTS

I would like to thank everyone who has supported me throughout my education. In particular, I would like to thank my advisor, Dr. Chia-Hsiang Menq, for his advice and ability to give just the right amount of direction. I have learned a great deal from him, both on technical subjects and on how to choose the right course of action.

I would also like to thank Dr. Yuan F. Zheng for sharing his experience and knowledge to offer a way through in the Image Processing part of his work. I would also like to thank Jayanth Gobbalipur Ranganath for doing a great job in training me for this work. I greatly appreciate his suggestions and friendship throughout the project. I'd like to thank Zhipeng Zhang and Peng Cheng for their key contributions to the hardware setup and the image processing software. To John, I extend many thanks for all his help and patience in fabricating the cantilevers used in this work.

I also appreciate the support and insight of fellow lab members Daisuke Matsuura and Yanan Huang. There fresh perspectives have helped me over many hurdles.

Finally, I thank all of my friends and family who have supported and encouraged me every step of the way. To my parents: thank you for everything!

VITA

October 24, 1985……..	Born – O.F. Itarsi, MP, India
June – August 2006……..	Summer Intern, General Electric GRC, Bangalore, India
June 2007…….	B.Tech. Mechanical Engineering, Indian Institute of Technology Madras, Chennai, TN, India
September 2007 – June 2009……...	Graduate Teaching Associate, The Ohio State University, Columbus, OH

PUBLICATIONS

Nagose, A., Somani A., Shrot, A. and Narasimhan, A., "Genetic Algorithm Based Optimization of PCM Based Heat Sinks and Effect of Heat Sink Parameters on Operational Time", *ASME Journal of Heat Transfer*, Jan 2008

FIELDS OF STUDY

Major Field: Mechanical Engineering

Studies in:

Control Systems	Professors C.H. Menq, V.I. Utkin
Dynamics	Professor Robert Parker
Fault Diagnosis	Professor Giorgio Rizzoni
Measurement Systems	Professor E.O. Doebelin

TABLE OF CONTENTS

LIST OF FIGURES

LIST OF TABLES

CHAPTER 1

INTRODUCTION

1.1 Multi-Axis Atomic Force Microscope

Atomic Force Microscope (AFM) is a versatile and a widely used instrument in nanotechnology [2]. It is a very high resolution type of Scanning Probe Microscope that not only provides topography of surfaces with nanometer and Angstrom resolution, but is also capable of nano-scale manipulation. It has found applications in the semiconductor industry, chemistry, biology etc.

The applications of AFM are limited by its inability to image the surfaces with large geometric variations. Hence it is effectively a two-dimensional (2D) surface tool [3, 4]. Although some custom shaped tips have been developed for certain specific surface profiles [5, 6], they are not three-dimensional in true sense. A conventional 2D AFM can be made a true three-dimensional (3D) surface tool by allowing the orientation of its scanning tip to be controlled. According to Jayanth et.al [1], this can be accomplished by attaching a magnetic particle on the head of a conventional AFM cantilever (AFMC), as shown in Fig. 1.1(a). Forces can now be applied to the AFMC by applying an external magnetic field using the two solenoids, resulting in bending of the AFMC along its

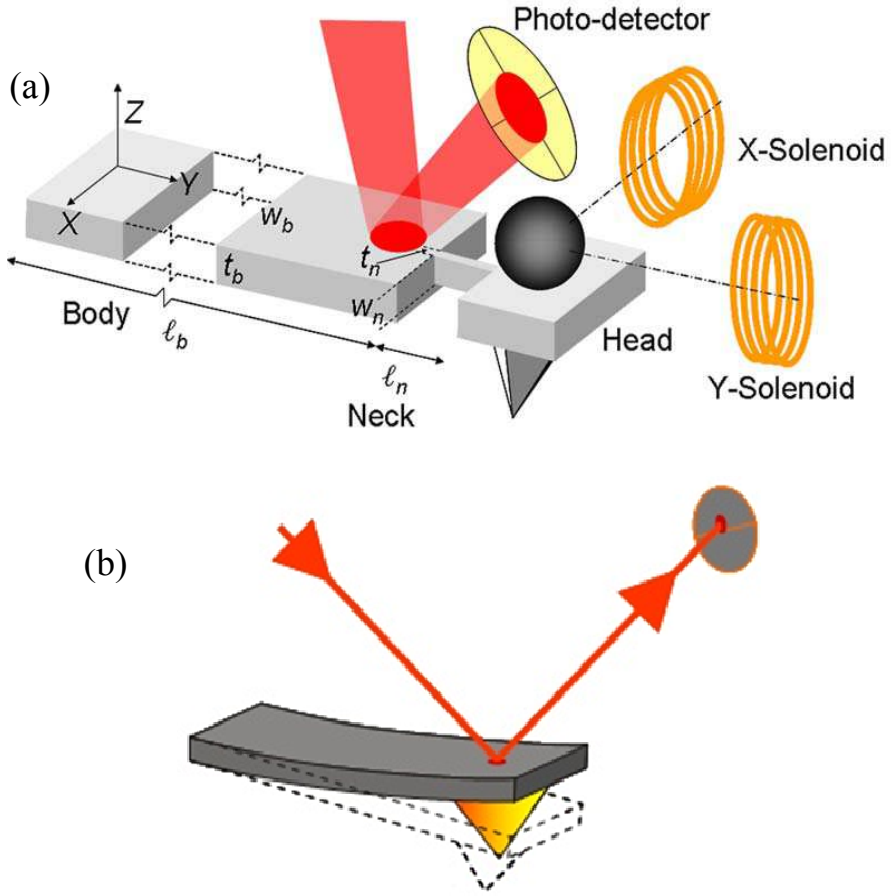

Figure 1.1 Comparison of AFM Cantilevers (a) Multi-axis [1] (b) Conventional

flexible neck. Thus by controlling the current passing through the two solenoids, tip orientation can be changed.

Only the conventional and custom-shaped AFMCs are available commercially. Thus a conventional AFM needs to be modified to create a multi-axis AFMC. First material is machined out using Focused Ion Beam milling to create the neck. Next a magnetic particle of appropriate size is glued to the AFMC at the desired spot.

1.2 Review of Current Particle Attachment Process

The dimensions of a typical AFMCs used are 150 × 40 × 6 μm. Although some are as long as 225 μm. Fig. 1.2 depicts the key steps in the particle attachment process when done manually. A short description of each step is provided next.

- Prepare micro-pipettes (MPs): This involves preparing two MPs to be fine enough to handle an object of size of a few micrometers. The MPs being used are manufactured by Sutter Instruments. They are hollow glass cylinders of 1.00 mm outer diameter. A single MP is pulled under heat using a Sutter P-97 Pipette puller. This causes it to elongate along the small heated region and

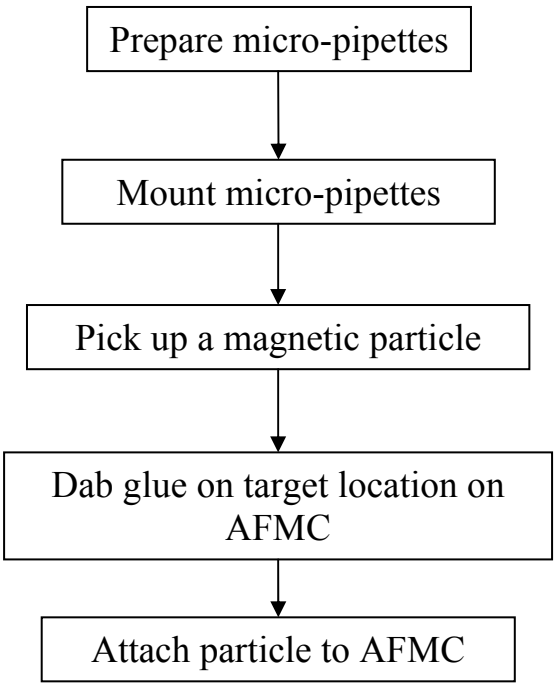

Figure 1.2 Block Diagram of the Manual Particle Attachment Process

ultimately break into two MPs with very fine tips. Tip remains hollow with an outer diameter of 1-5 μm. One of these fine tip MPs is then brought close to a heated filament using Narishige's MF-900 Microforge, which causes it to bend slightly. This slight bend is necessary to pick up a particle from anywhere on a flat surface, without touching any other part of it.

- Mount micro-pipettes: Two MPs need to be mounted on the motion stage. One is used to hold the glue, while the other is used to hold a magnetic particle. These are mounted side-by-side to reduce the amount of movement required during the process.
- Pick up a particle: First a mica sheet is prepared by removing its top layer. This can be done by simply using an adhesive tape. It reduces the contact force between the particles and the surface, making it easier to pick them up. A little bit of magnetic powder is then poured over this surface. Tip of one of the micro-pipettes is moistened using certain viscous fluid. A small amount of any oily substance is usually enough. A particle of roughly the desired size is then chosen. The desired radius is between 20-70 μm, and depends on the desired multi-axis AFM performance. The MP is then maneuvered over the surface, while it is observed under Stemi SV-11 APO microscope. Using the manually controlled motion stage, the particle is then picked up using the tip of MP.
- Glue the desired spot: Cantilever is brought under the focus of microscope. The second MP is used to dab sufficient glue at the target spot on the

cantilever. Again the motion stage is actuated manually to control the position of the MP.

- Attach particle: Particle is then brought in contact with the target location dabbed with glue. The AFMC surface is highly reflective. The reflection of the particle can be seen on it. The separation between the particle and its reflection indicates the vertical distance between the particle and AFMC. The contact with the cantilever is confirmed when the cantilever bends slightly. This is signaled by the change in brightness of the AFMC. When the particle has been successfully attached, MP is moved laterally outwards, so that there is minimum external force on the fragile AFMC due to adhesion between MP and glue.

1.3 Objective

The objective of this work is to automate the particle attachment process as much as possible. As the travel range of the piezo stage used is limited, some manual intervention would still be required. So the automated process for each of these steps is divided into 2 parts: initial manual manipulation and automated stage. First part would involve bringing the object close enough to the target location, after which the automated stage will take over. While a few other steps, e.g. MP preparation, would still be completely manual. A visual feedback controller will be used to actuate the piezo-actuator. The images for visual feedback are provided by a camera attached to the

microscope. As only one camera is being used, stereovision cannot be used to extract the absolute location.

The developed process should be robust enough to tackle the varying conditions and the different user requirements, such as different particle sizes. It should also be robust against the inherent vibration in the system. The primary objective is accomplished through the following intermediate objectives:

- Design a setup to perform the automated particle attachment process using visual feedback
- Develop robust image processing algorithms capable of extracting the required information from the images acquired for the majority of the possible cases
- Derive a model of the setup which would estimate position based on the feedback from a single camera
- Develop a control strategy which is faster and more accurate than the current manual process
- Perform calibration to derive system parameters necessary for the model and the control strategy developed
- Implement the automated process in experiments for proof-of-concept.

The focus of this work will be on automating the actual particle attachment step. It will be referred to as the 'attachment step' in this document hereafter. The developed controller and the image processing algorithms based only on a single camera, can serve as a foundation for similar other applications. It will be extended to support a few other

steps in this process as required. Hereafter references to ‘the process’ would denote the particle attachment process, unless otherwise specified.

1.4 Motivation

The motivation of this work is to make this entire process easy on the user. The manual process described earlier can be very taxing. One of the main problems is the inherent vibration in the system. This requires users to be very still while manipulating the motion stage to reach the target location. Even a small jerk while performing the task can cause unnecessary vibrations. It could result in some damage, like the particle being dropped from the tip of MP.

Additionally the motion stage needs to be manipulated very carefully. The resolution of the screw gauges used is 0.0001 in, while the width of the cantilever is itself around that size. Thus the accuracy of target location may be compromised. Also when the particle is very close to the AFMC, a slightly larger turn on the screw can be enough to break it. This is highly undesirable because of the high costs of AFMCs used. Hence it becomes very critical to perform the process slowly and carefully. Sometimes users have to hold their breaths for the duration of the process, which can be a tough job to do.

A few steps in this process need to be automated to make it faster, more accurate, more comfortable for the user and eliminate the chances of causing any damage. They are the ones which require fine manipulation. The following stages were identified as the ones that need to be automated:

- Picking up the particle
- Dabbing glue on to the target location
- Attaching the particle

All the three of these steps require manipulation of the motion stage. With the hardware being used, it would be impossible to completely eliminate manual involvement even in these steps. But the role of the user would now be limited to getting the object within the range of piezo-actuator. It is more comfortable for user, as there is much less chance of any damage and accuracy is not that important.

1.5 Organization of Thesis

Chapter 2 describes the design of the setup used in this work. The key components include a piezo-actuator, a manually actuated motion stage, two MPs, an AFMC, a microscope and a CCD camera. The relative placement of these components is described. And a model for the image formation process is derived.

All the image processing used in this work is described in Chapter 3. It includes extraction of the location, and the motion if applicable, of a particle, cantilever and a MP, from the images captured. An algorithm to deal with undesired vibrations is presented.

The development of control strategy is the emphasis of Chapter 4. An image location based approach is developed to manipulate the piezo-actuator. Additionally path planning is done for the attachment step. And conditions are described to trigger the process off.

The results of the control strategy as implemented in experiments are presented in Chapter 5. Calibration of the system parameters that vary from one experiment to other is described.

The final chapter, Chapter 6, contains conclusions on the automated attachment magnetic particle process developed in this thesis and suggestions for future work.

CHAPTER 2

SETUP DESIGN AND MODELING

2.1 Introduction

Since the main focus of this work is on automating the attachment step, the setup is first designed to facilitate it. After which the setup is extended to perform the rest of the steps and make the transitions from one step to another as smooth and less time consuming possible.

This chapter begins with the design of the physical setup for the attachment step. Physical setup refers to relative placement of everything but the optical components. The logic used for the design process is presented. The microscope and illumination is next designed based on the physical setup. A few modifications required to perform rest of the steps in the process. An image formation model is derived to relate the real world to the image pixels. The chapter concludes with a brief summary.

2.2 Physical Setup for the Attachment Step

A Stemi SV11 microscope forms the core of the setup. Objects that need to be observed or controlled at various steps of the process should be within the focal range of the objective. For the final step this constitutes the magnetic particle and AFMC. The latter is fixed at the focal plane of the objective. The target location is on the top surface of the rectangular AFMC, as shown in Fig. 2.1. The exact position depends on the performance requirements out of that AFMC when used in a multi-axis AFM. But usually it is very close to the tip of AFMC.

The particle is held at the tip of a MP, as shown in Fig. 2.2(a). The MP holds the

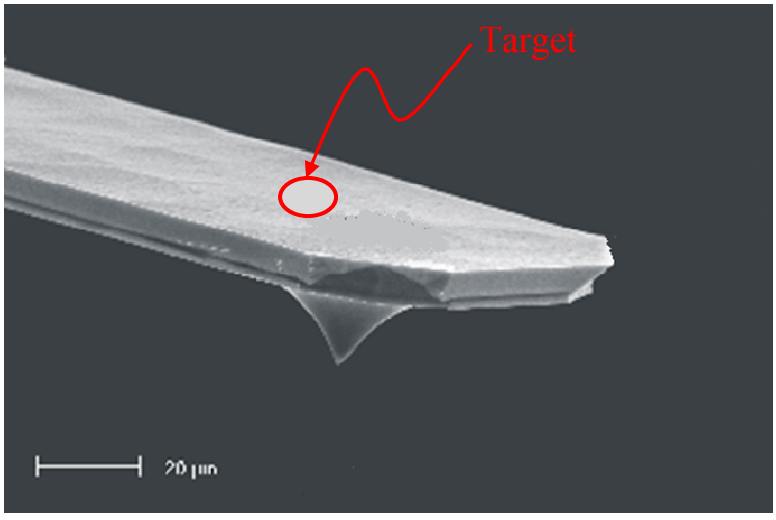

Figure 2.1 Scanning Electron Microscope (SEM) image of an AFM. The usually desired target location is indicated on the top surface

particle at its tip. It is aligned so that it does not block the tip of AFMC from being visible. The MP is to be maneuvered to bring the particle towards the target location manually or automatically. The automated stage used is Nanocube, made by Physik Instrumente. It is a three-axis piezo-stage, with the travel range of 100 × 100 × 100 μm. This is not enough to automate the process completely. Thus Nanocube is placed on top of another motion stage which is actuated manually using the three screw gauges, as shown in Fig. 2.3. This is made easier due to the compactness of Nanocube. In fact it measures only 44 × 44 × 44 mm. The total travel range now is about 10 cm in each direction.

The particle is a dark spherical blob when seen under the microscope. It can only be seen when the background is illuminated. This can be achieved by implementing transmitted light illumination. In the attachment step, the particle is supposed to be right above the AFMC. And it will block the particle partially by its shadow, if only transmitted light illumination is used. This is unacceptable if the diameter of the particle is close to the width of AFMC.

The AFMC being used have a highly reflective top surface, which enables it to reflect the laser during the operation of AFM. This makes it suitable for reflected light illumination. When the particle is right on top of the cantilever, the AFMC in the background would be illuminated making the dark particle visible again. But reflected light illumination alone is not the solution, as the particle would be indistinguishable in any region but on top of AFMC.

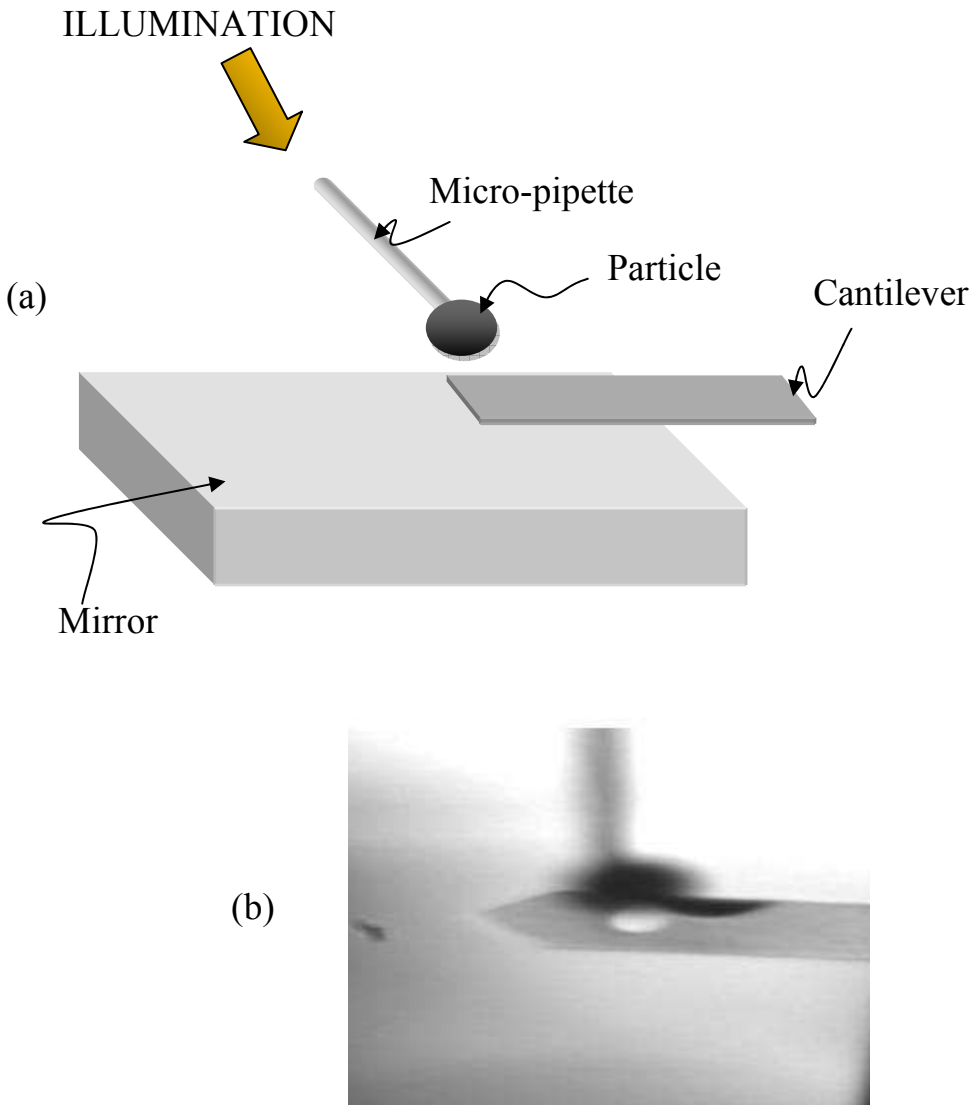

Figure 2.2 Scene setup for the Particle Attachment Process (a) Schematic. NOT TO SCALE (b) Scene when viewed from the microscope

The proper illumination should be a mix of both, providing transmitted and reflected light. A mirror placed below the AFMC, and illuminated from above, as shown in Fig. 2.2(a), seems to satisfy all the requirements. As can be seen from a sample image

in Fig. 2.2(b), it provides reflected light to see the particle while it's away from AFMC. And when it is closer, AFMC surface acts as the mirror to provide an illuminated background.

The physical setup has been photographed in Fig. 2.3 below. The AFMC is too small to be seen in this view.

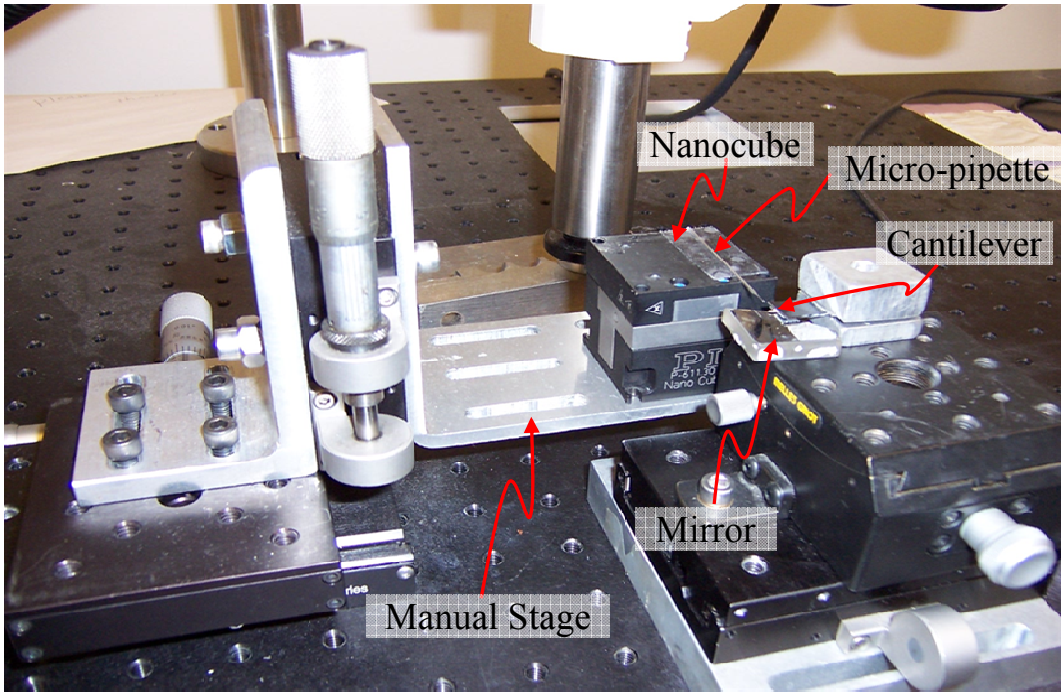

Figure 2.3 Complete Physical Setup for the Particle Attachment Process

2.3 Optical Setup for the Attachment Step

The Stemi SV11 microscope used in this work is a stereomicroscope employing the telescope concept, as shown in Fig. 2.4(a). Two microscope systems are arranged in

parallel and share a common objective. The stereo angle is formed by the extra-axial pairs of rays. Using it in stereo-mode would require external source of illumination, e.g. a four-point ring illuminator. Since the setup designed works on the light reflected off the mirror and AFMC, each bundle would need to be oriented such that when the reflected

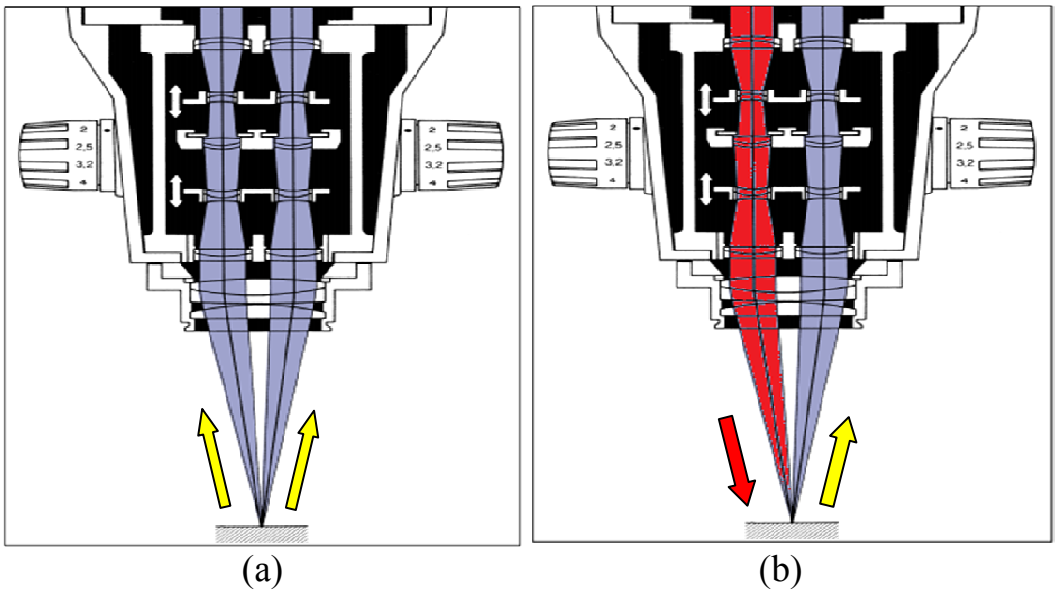

Figure 2.4 Optical path for the Stemi SV11 microscope (a) Original stereomicroscope (b) Modified microscope

light enters the objective. Both AFMC and the mirror would need to be reoriented too. This is difficult given the way AFMC is placed on the setup.

AFMC is almost horizontal by default. The only way reflected light can enter one objective path is if it is coming from the other objective path. This is shown in Fig. 2.4(b). Hence the optical tube was connected to the left optical path. And the reflected

light can be seen from the right eyepiece. It is no longer a stereomicroscope, as only one view can now be viewed and recorded.

The light source is an Ace Halogen manufactured by Schott Fostec. It is attached to the microscope on the left camera adapter, as shown in Fig 2.5. The incident light should follow the exact optical path, although in reverse direction. A Hitachi KP-M1 Charge Coupled Device (CCD) camera captures the reflected light from the right camera adapter.

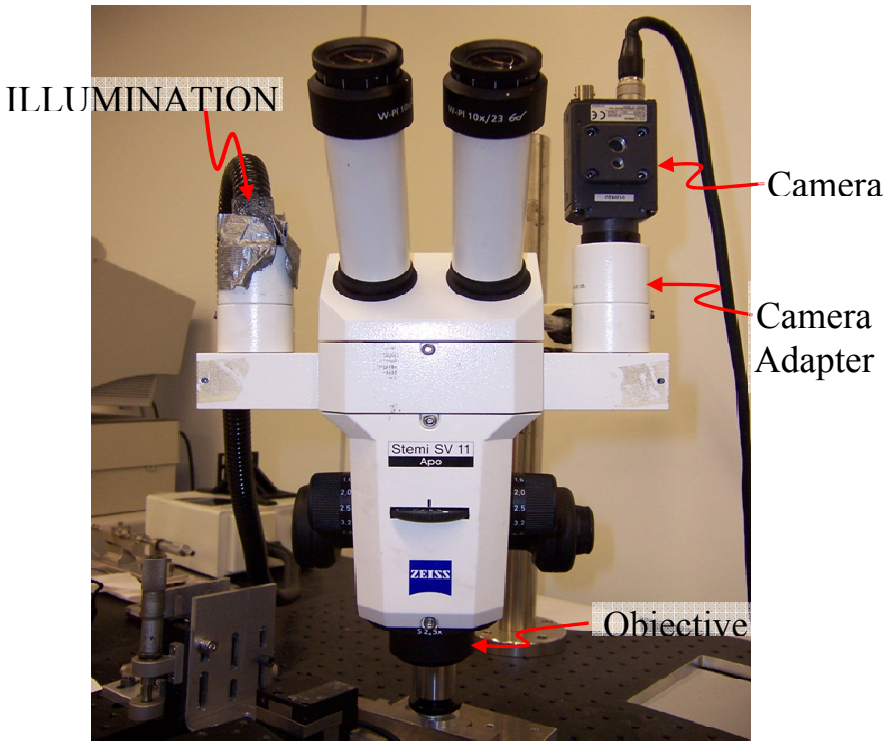

Figure 2.5 Optical Setup for Particle Attachment Process

A Matrox frame grabber captures the data from the camera to be used in image processing, while the control output is sent to the Nanocube through the DA converter from Measurement Computing and a Piezo-amplifier.

2.4 Modified Setup for Other Steps

The optical setup remains the same throughout the process. Only slight modifications are made to the physical setup to perform the rest of the steps. The transition from one step to another should be as smooth and less time consuming as possible. This is especially important when the cantilever has been dabbed with glue and there is small time window to attach the particle before the glue sets.

The MP preparation does not require this setup. Mounting one of the MPs has been described in Sec. 2.2. The other MP which holds the glue should be close to the first one. This would reduce the amount of movement required to get ready for the attachment step. This is critical as there is limited time available before the glue sets. Glues with wide range of settling times are available, though.

The particle pickup step requires the mica sheet which holds the magnetic particles to be under the microscope. Once the particle has been picked up, the mica sheet is manually moved away and the AFMC is brought under the microscope. Care must be taken not to knock the AFMC to rest of the setup. The microscope sometimes needs to be refocused, as the AFMC may not be the same height as the mica sheet, though this does not require a lot of effort.

2.5 Image Formation Model

Every location in the Real World Coordinate System (RWCS) has a point on the image coordinates corresponding to it, although it can be seen only if it is in the field-of-view. Through image processing, the locations of different object in the image frame would be found out. In order to manipulate these objects in the real world, it is important

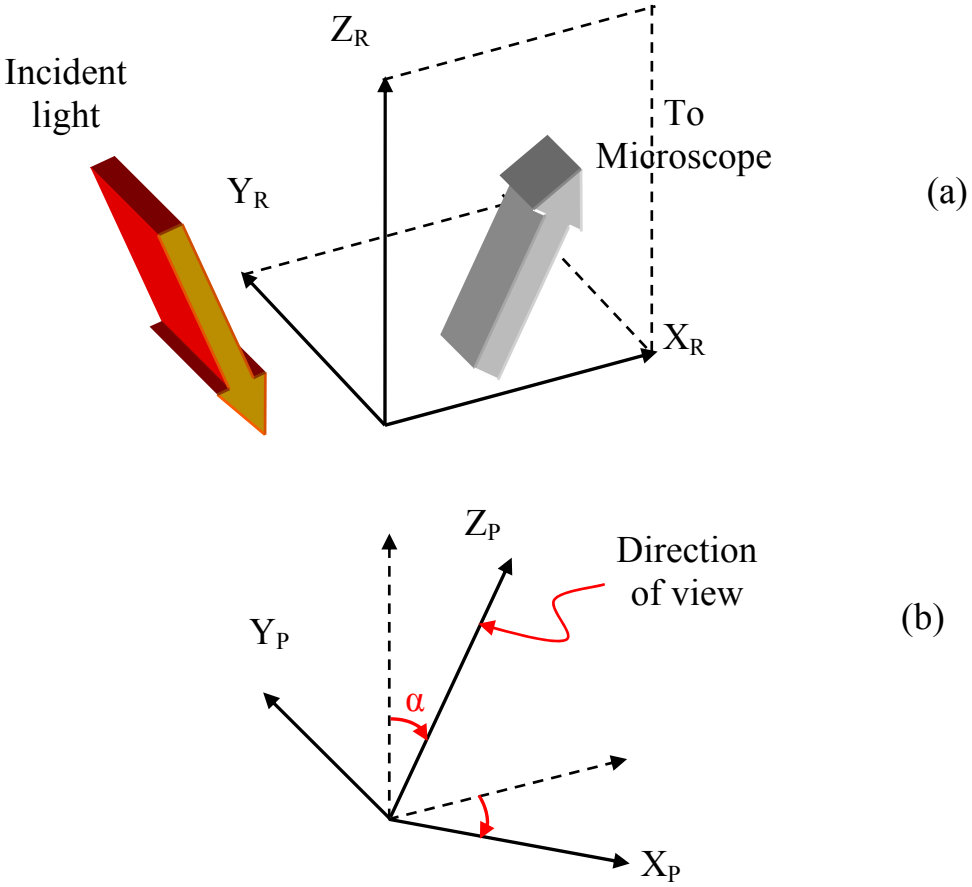

Figure 2.6 (a) Real World Coordinate System (b) Projected Coordinate System

to have a model relating the two coordinate frames. Now that the relative placement of all the components is known, the image formation process can be modeled.

The RWCS is fixed to any distinguishable feature of the scene which is captured by the camera and does not move during the process. AFMC remains fixed during the attachment step and in-focus too. Additionally the particle needs to be manipulated in the neighborhood of the tip. For the attachment step, tip of the AFMC is a good candidate for the origin of RWCS. For other steps any similar features can be chosen.

The orientation of the RWCS ($\vec{X}_R$) is determined by the direction of illumination. Incident light and direction from which the scene is viewed by the microscope, as shown in Fig. 2.6(a), both lie in the vertical x-z plane. z-axis is pointing vertically upwards, while x-axis lies in the horizontal plane. Direction of view is inclined at the semi-stereo angle (α) to the z-axis along the vertical x-z plane. It is a system constant. Light is incident at the same angle to the vertical direction.

The RWCS is first transformed by the semi-stereo angle (α), as shown in Fig. 2.6(b). This angle is a system constant and can be calibrated if accurate vertical displacement is generated. The new projected coordinates ($\vec{X}_P$) are given by

$$\vec{X}_P = \begin{bmatrix} \cos\alpha & 0 & -\sin\alpha \\ 0 & 1 & 0 \\ \sin\alpha & 0 & \cos\alpha \end{bmatrix} \vec{X}_R \tag{2.1}$$

This then passes through the optics of the microscope and gets magnified ($\vec{X'}_P$).

$$\vec{X}'_P = M\,\vec{X}_P \tag{2.2}$$

$$M = M_1 M_2 M_3 = 2.5 \times m \times 1$$

where M_1 is the magnification of the objective (2.5x), M_2 is the magnification of the body (0.6 - 6.6x) and M_3 is the magnification of the camera adapter (1x). The attachment step is always done at the highest magnification, $M = 13.5$.

The magnified image is then projected on to the CCD chip of the camera, hereafter referred to as simply CCD. Modeling of this part has been divided into two parts. First, the view is projected on a hypothetical image frame ($\vec{U}_M$) with same pixel pitch as the actual camera, whose origin coincides with the point where the origin of the RWCS is projected to. As shown in Fig. 2.7(a), this hypothetical image frame is in

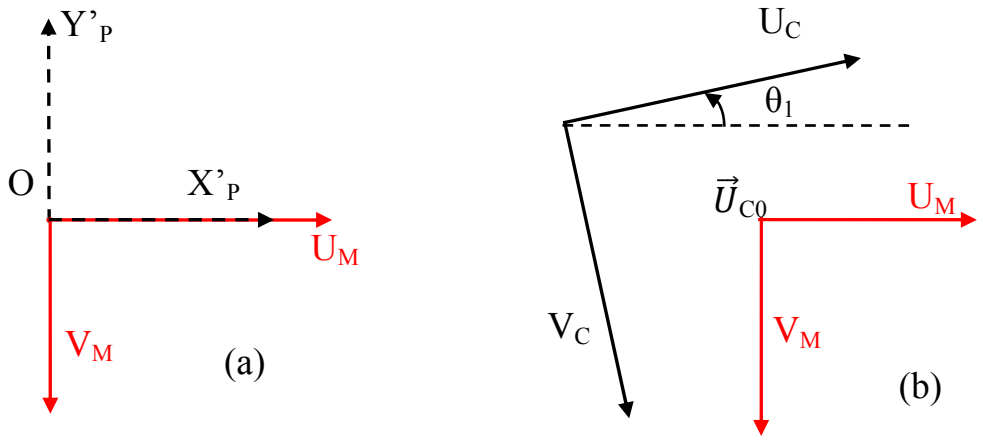

Figure 2.7 Camera coordinate frame (a) Magnified projection coordinate system to Hypothetical image coordinate system (b) Hypothetical camera coordinate system to Real camera coordinate system

perfect alignment with the projection of the RWCS. They are related by the pixel pitch (c) of the CCD. For the Hitachi KPM1 camera it is 11 μm/pixel.

$$\vec{U}_M = \begin{bmatrix} 1/c & 0 & 0 \\ 0 & -1/c & 0 \end{bmatrix} \overrightarrow{X'}_P \tag{2.3}$$

Next this hypothetical image frame ($\vec{U}_M$) is mapped to the actual image frame ($\vec{U}_C$), as shown in Fig. 2.7(b). Ideally if the camera fits into the adapter properly, θ_1 is zero. But the wear and tear in the threads leads to an improper alignment, causing this change in orientation. Secondly the origins do not coincide. Since a visible feature of the scene was chosen as the origin of RWCS, its location on the image ($\vec{U}_{C0}$) can be found from image processing. Lastly the Hitachi KPM1 is an interlaced grabbing camera. Due to the reasons which will be explained later in Chapter 3, only 1 field is grabbed. This halves the resolution along v_c. Thus in homogenous coordinates:

$$\begin{bmatrix} u_C \\ 2v_C \end{bmatrix} = T\left(\begin{bmatrix} u_{C0} \\ 2v_{C0} \end{bmatrix}\right) R(-\theta_1)\vec{U}_M$$

$$\begin{bmatrix} \vec{U}_C \\ 1 \end{bmatrix} = \begin{bmatrix} cos\ \theta_1 & -sin\theta_1 & u_{C0} \\ \frac{1}{2}sin\theta_1 & \frac{1}{2}cos\theta_1 & v_{C0} \\ 0 & 0 & 1 \end{bmatrix} \begin{bmatrix} \vec{U}_M \\ 1 \end{bmatrix} \tag{2.4}$$

The entire image formation process has been derived in Eq. 2.1 - 2.4. Combining Eq. 2.1-2.3 gives

$$\vec{U}_M = \frac{M}{c}\begin{bmatrix} cos \propto & 0 & -sin \propto \\ 0 & -1 & 0 \end{bmatrix}\vec{X}_R \tag{2.5}$$

Lastly the RWCS ($\vec{X}_R$) needs to be related with the Nanocube Coordinate System ($\vec{X}_N$). If the Nanocube is place on the manual stage properly, the vertical directions of the two coordinate systems are almost perfectly aligned. But the other two axes may not be aligned, and it changes from experiment-to-experiment. The orientation between the two sets of axes needs to be calibrated before performing every experiment. Additionally the Nanocube follows a left-handed coordinate system, as can be seen from Fig. 2.8. The relation is given by:

$$\begin{bmatrix} \vec{X}_N \\ 1 \end{bmatrix} = \begin{bmatrix} -cos\theta_2 & sin\theta_2 & 0 & x_0 \\ sin\theta_2 & cos\theta_2 & 0 & y_0 \\ 0 & 0 & 1 & z_0 \\ 0 & 0 & 0 & 1 \end{bmatrix}\begin{bmatrix} \vec{X}_R \\ 1 \end{bmatrix} \tag{2.6}$$

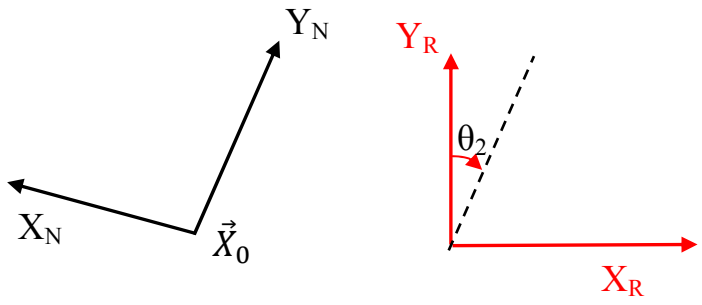

Figure 2.8 Nanocube Coordinate System and RWCS

The Eqs. 2.4 – 2.6 provide a complete model for the image formation from the Nanocube position to the actual image pixel.

2.6 Summary

This chapter describes the design of a complete setup to perform the process and the logic behind it. The complete system was divided into optical and non-optical parts, and designed separately to satisfy all the requirements. An image formation was also derived, relating the RWCS to the corresponding image pixels. The next chapter deals with image processing algorithms to locate various objects and extract other relevant information from the images captured using this setup.

CHAPTER 3

IMAGE PROCESSING ALGORITHMS

3.1 Introduction

This chapter begins with the description of the vibration elimination from the images captured. Next the image processing algorithms for each of the objects is described separately. The main objective is to find the locations of these objects in the image. In this chapter, 'AFMC' refers to the AFMC region in the image captured. The same holds true for 'particle' and 'MP'. 'Reflection' refers to the reflection of the particle on AFMC surface. 'Tip of AFMC' refers to the shortest edge of AFMC, while the two longer edges are simply referred to as 'edges of AFMC' or simply 'the edge'. The tip happens to be close to the actual tip used for AFM operation. And 'intensity' refers to the grey level of that point or region.

3.2 Vibration Elimination

The microscope system has inherent vibrations. As the system is not mounted on an optical table, any light touch causes the images captured to be blurred due to the

vibrational motion. When the system is operating under a controller, this vibration of about 5 μm amplitude is not much of a problem, as it is compensated for by the control output. But other steps, like the calibration for system parameters, are sensitive to vibration. And it is important to reduce its effect as much as possible.

The Hitachi CCD camera provides interlaced images. All the pixels are not captured at the same instant of time. Two sets of alternating rows are captured at slightly different times to form one frame. And it shows a pattern, like shown in Fig. 3.1(a), when the object being recorded is moving. De-interlacing seems to get rid of this issue, but at

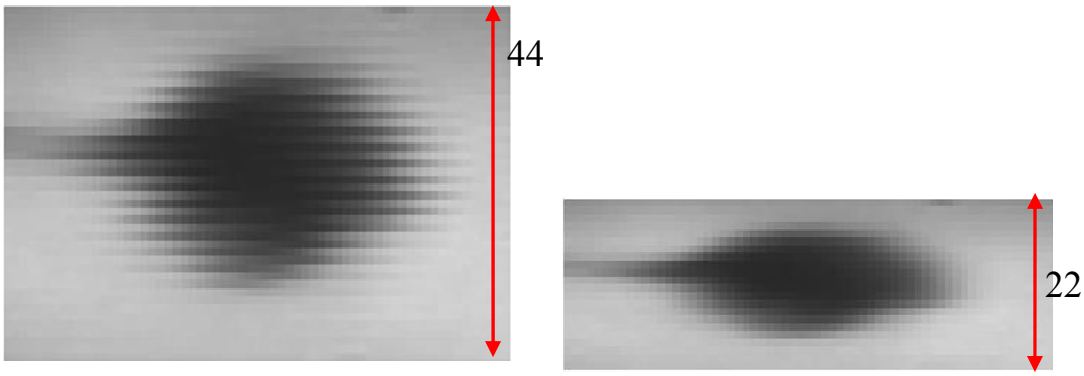

Figure 3.1 Motion Blur due to vibration (a) Interlaced (b) De-interlaced. Vertical resolution in pixels is indicated.

the cost of lower resolution in one direction. Now the objects only seem to spread-out due to the motion blur, as can be seen in Fig. 3.1(b). All the images captured are automatically de-interlaced from now on. Due to the reduced resolution along the vertical direction, shapes would appear distorted, e.g. a circular particle would appear elliptical.

When the particle/AFMC size needs to be found out, it is important to use the image with the least amount of motion blur. The calibration process of system parameters is also very sensitive to vibrations. It is important to reduce the effect of motion blur in such cases. Various Focus Measures (FMs) were tested for this very purpose. The FM chosen should be highly sensitive to motion blur and computationally fast enough. A few basic FMs [7] were tested and the results have been compared in Table 3.1 below. They are computed on image grey levels. Three images with different level of motion blur were used for comparison. $F_1, F_2$and F_3 correspond to FM on the image with no blur, low blur and high blur respectively. The image used was 200 × 250 pixels.

Table 3.1 Comparison of Focus Measures against motion blur

FM	Definition	Computati-onal Time (10^{-5} s)	F_2/F_1	F_3/F_1
Variance	$\iint (g(u,v)-\mu_i)^2 dudv$	8	0.99	0.54
l_1 norm of gradient	$\iint \left\|\frac{\partial g(u,v)}{\partial u}\right\| + \left\|\frac{\partial g(u,v)}{\partial v}\right\| dudv$	52.1	0.98	0.87
l_2 norm of gradient	$\iint \left[\frac{\partial g(u,v)}{\partial u}\right]^2 + \left[\frac{\partial g(u,v)}{\partial v}\right]^2 dudv$	54.1	0.94	0.34
l_1 norm of Laplacian	$\iint \left\|\frac{\partial^2 g(u,v)}{\partial u^2}\right\| + \left\|\frac{\partial^2 g(u,v)}{\partial v^2}\right\| dudv$	85.1	0.93	0.66
Energy of Laplacian	$\iint \left[\frac{\partial^2 g(u,v)}{\partial u^2} + \frac{\partial^2 g(u,v)}{\partial v^2}\right]^2 dudv$	87.3	0.85	0.35

The smaller F_2/F_1 and F_3/F_1 are, the more sensitive the FM is to the low and high motion blurs respectively. As can be seen from Table 3.1, all the FMs respond well to high motion blurs in the images. But only the one based on Energy of the Laplacian responds well to the low motion blur. Although it takes maximum computational effort, the computational time will still be very small compared to rest of the image processing algorithms. Hence this FM was used on every image grabbed and the best image was regarded for the vibration sensitive image processing.

3.3 AFM Cantilever

The location of the AFMC is required for the attachment step. It would automatically define the region in which particle's reflection would be visible. It is also important if the target location is specified with respect to its tip. Also the region along the boundaries of the AFMC would produce a high-gradient background, which might confuse the particle tracking algorithm. Hence the information from close to the edges needs to be discarded.

3.3.1 Challenges

The AFMC remains fixed throughout the attachment step. Thus determining its location initially would suffice. The algorithm needs to be robust against the intensity of the AFMC and background intensity. As the illumination intensity varies from experiment-to-experiment, the algorithm should be robust against background intensity. Robustness against AFMC intensity is also required, as it changes when AFMC is not

perfectly horizontal, which alters the amount of light being reflected in the direction of view. The optical path is fairly clean, but still a few dust speckles can be seen on all the images captured. The algorithm should be robust to these speckles too, even if they interfere with the AFMC region. The width of AFMC is unknown and varies.

3.3.2 AFMC Detection

The AFMC detection has been divided in two parts: edge detection and tip detection. Fig. 3.2 shows a block diagram of the AFMC detection algorithm. It assumes that AFMC cuts through the right edge of the image and is located approximately in the center vertically. An image with poor contrast is selected to demonstrate the algorithm

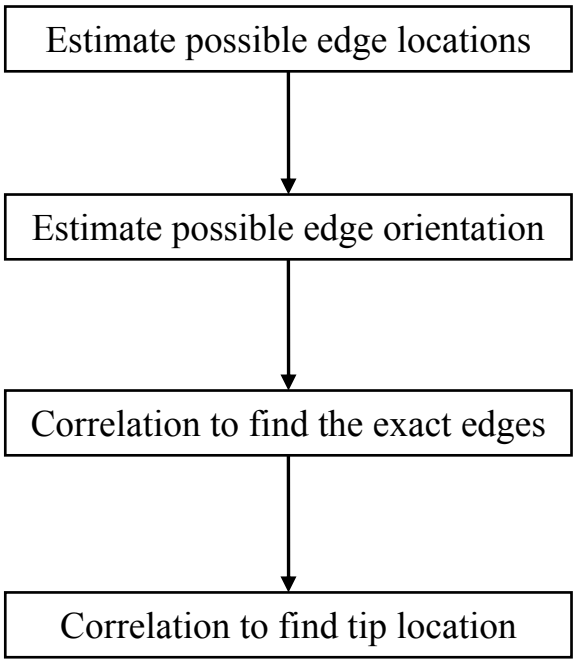

Figure 3.2 Block Diagram of the AFM Cantilever Detection Algorithm

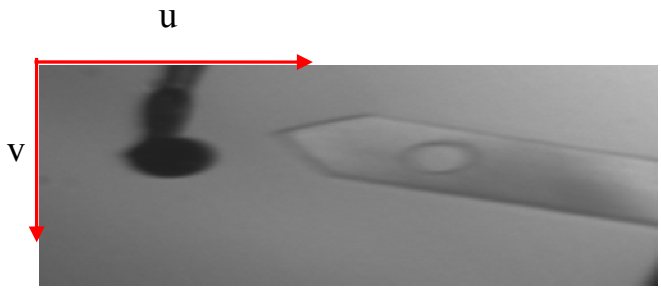

Figure 3.3 Image used for demonstration. It has poor contrast.

and its robustness. The image used is shown in Fig. 3.3.

The edge is located where the maximum gradient occurs in the image or the Laplacian is zero. To keep the algorithm insensitive to the actual intensities, the image gradient is correlated with a gradient template of an ideal edge. If $f(u,v)$ is the image of size M×N. is correlated with the gradient template $g(u,v)$, the correlation measure ρ_{fg} is given by:

$$\rho_{fg} = \sum_{u=0}^{M-1} \sum_{v=0}^{N-1} \left|\vec{\nabla} f(u,v)\right| g(u,v) \tag{3.1}$$

The solution space for the each edge consists of two parameters: location of edge and its orientation. Correlation is used to determine the exact solution. The template models the Gaussian blur about the edge and is defined by: the point it passes through (u_0, v_0) and orientation $(\emptyset)$.

$$g(u,v) = e^{-\frac{d^2}{2\sigma^2}} \tag{3.2}$$

$$d = \frac{|mu - 2v - mu_0 - 2v_0|}{\sqrt{1+m^2}}$$

The location of edge is measured along a column close to the right edge of the image. The correlation function, given by Eq. 3.1, has been evaluated and plotted in Fig. 3.4 for the entire solution space. And the two highest peaks correspond to the two edge locations. Since the edges are parallel, the two peaks have the same orientation. Since the solution space is huge and mostly zero, a rough estimate of the two parameters would narrow down the search for the solution to a very small region and greatly improve the computational effort required.

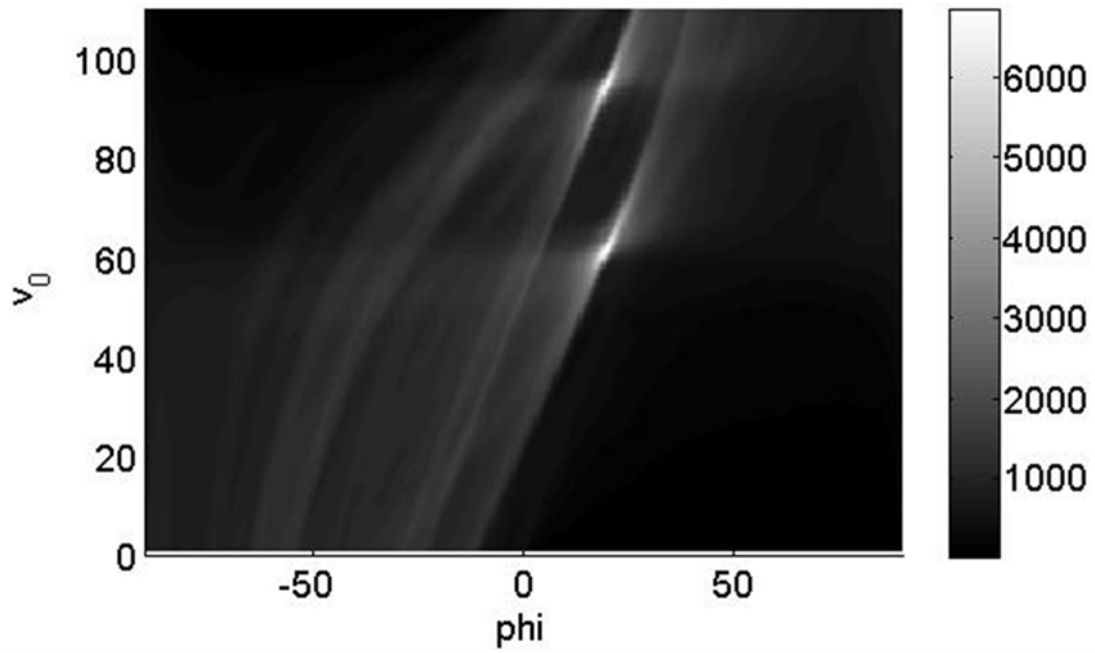

Figure 3.4 Correlation measure evaluated for the entire Solution space of AFMC edges

A column is chosen close to the right edge of the image. A pixel from every patch of high gradient along that column is entered into a list of possible edges. The threshold for the gradient is kept pretty low so that edges are captured even under low contrast. It would increase the speckles and any other external object that get recorded as possible edges. But they will be eliminated when exact edges are calculated. It's a small price for a more robust algorithm.

Next the approximate orientation is determined by finding the two-dimensional Fourier Transform (FT) of the image gradient, in Eq. 3.3. As the image gradient will be windowed before FT is applied, the AFMC should be roughly in the middle of the image.

$$F(\omega_u, \omega_v) = FT\left[\,\left|\vec{\nabla} f(u,v)\right|\right] \tag{3.3}$$

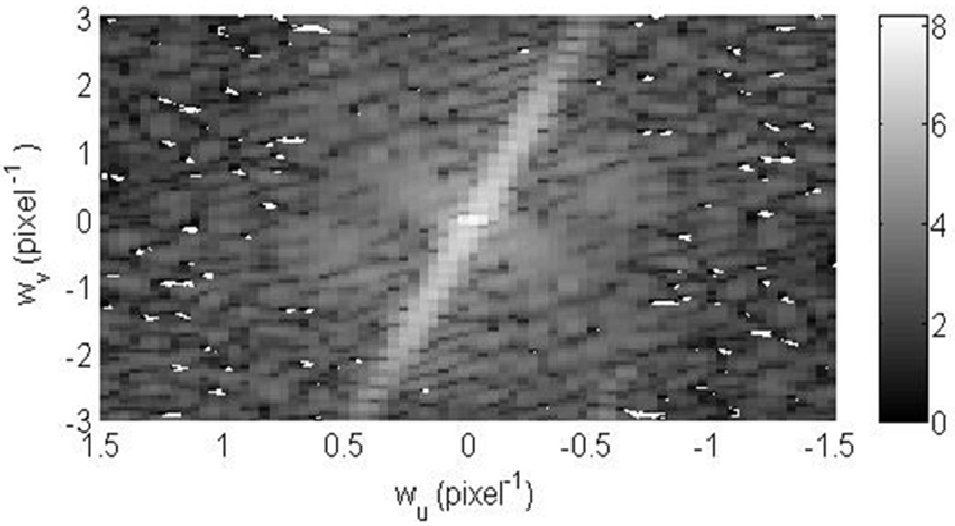

Figure 3.5 Log of Fourier Transform of Image gradient. x-axis has been reversed for an easier comparison with the image.

The FT is supposed to have peaks along the normal to the edge orientation. The magnitude of $F(\omega_u, \omega_v)$ has been plotted in Fig. 3.5.

Using the approximate orientation and possible edge locations found, the exact edges are determined by gradient climbing approach, i.e. simply moving in the direction of the gradient of correlation measure in the solution space, until the peak is reached. As can be seen from Fig. 3.4, the peak occurs on a hill which is really sharp along one direction. If the neighborhood search approach is used with a resolution which is not small enough, the algorithm may stop way before the actual peak is reached. This behavior has been observed with a resolution of 0.1 pixels. And that's why a gradient climbing approach is preferred.

The actual edges are separated from the artifacts by comparing their correlation measures. Sub-pixel accuracy can be achieved using this method. It was set at 0.1 pixels for this demonstration. The results for the image in Fig. 3.3 are tabulated in Table 3.2.

Table 3.2 Approximate and exact edges for Fig. 3.3

Approximate Edges		Exact Edges	
v_{0i}(pixels)	$\emptyset_i$(degrees)	v_0(pixels)	$\emptyset$(degrees)
49	18.14	46.2	17.1
80	18.14	80.9	17.2

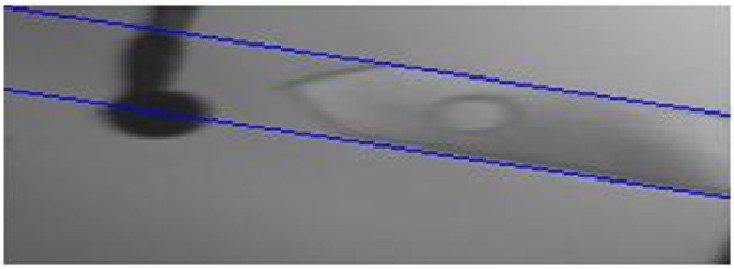

Figure 3.6 AFM Cantilever Edges

The approximate values found out are pretty close to the exact values. The edge orientation, found out independently for each edge, is pretty close, which is expected as the edges are parallel to each other. The exact edges have been plotted in Fig. 3.7.

The last step in the AFMC detection algorithm is to locate the tip. All the AFMCs

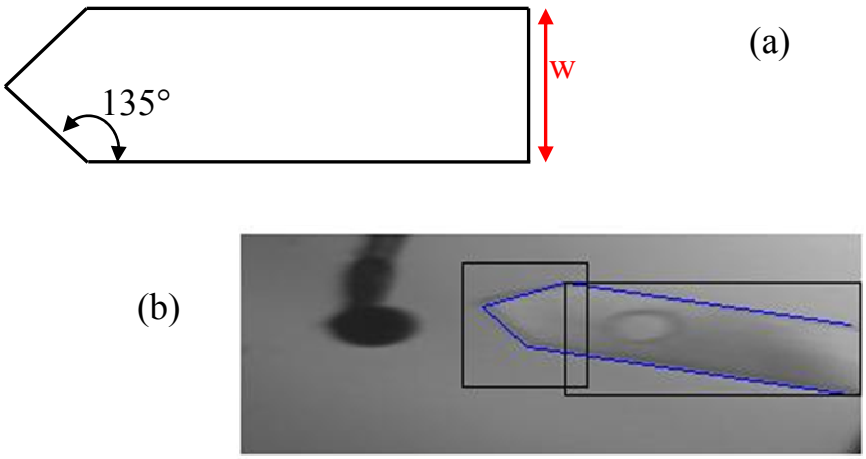

Figure 3.7 (a) Tip geometry for the AFM Cantilever (b) AFM Cantilever located by the AFMC detection Algorithm

have similar tip geometry as shown in Fig. 3.6(a). A correlation measure similar to Eq.3.1 and Eq. 3.2 is used. The region between the two edges is scanned for a peak in the correlation measure. There is only one degree-of-freedom, as the tip is symmetrical. Since the AFMC may not be perfectly horizontal its tip may look slightly sharper. The AFMC located after all this processing is shown in Fig. 3.6(b). After the AFMC has been located completely, two regions are automatically assigned. One surrounds the tip of AFMC and the other reflective region of AFMC, as shown in Fig. 3.6(b). Both of these are used later in the image processing.

3.3.3 Tip Deflection

AFMC is very flexible and fragile. Any external bending force must be limited so

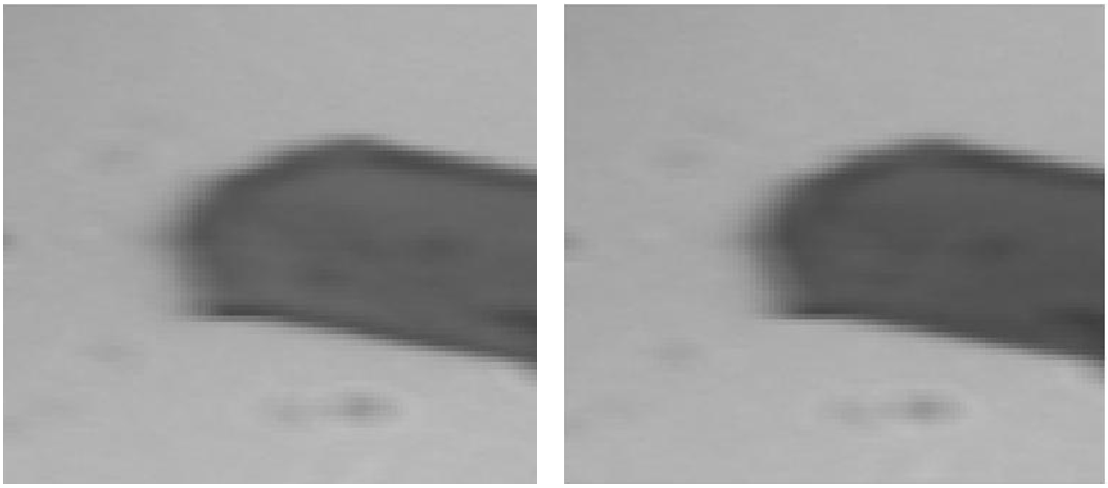

(a) (b)

Figure 3.8 Tip Region (a) Normal (b) After bending: Very slightly blurred. It is almost indistinguishable to the naked eye, but not the image processing algorithms.

that no damage is caused to the AFMC. During the attachment step, when the particle and MP is being brought down towards the target location, the MP may bend AFMC once the contact is made. Thus a trigger is required which would go off whenever the AFMC is bent. This could also act as a trigger to set the process off.

As can be seen from Fig. 3.8, if the AFMC was focused properly to begin with, once it bends, the tip shows the maximum deflection and is blurred in the image. This blur can be detected using an appropriate FM on the tip region from Fig. 3.7 (b). A few desired properties of an appropriate FM would be:

- Robust to the particular structure of an image such as brightness and noise
- Monotonic with respect to blur: The more blurred an image is, the smaller the value of the image focus measure should be.
- The focus measure must be unimodal, that is, it must have one and only one maximum value.
- Large variation in value with respect to the degree of blurring. Large usable range has a positive effect on the accuracy of the measure
- Minimal computation complexity

Some of these requirements have been already described in Section 3.2. In addition to the FMs defined in Table 3.1, another FM will be evaluated in the context of tip bending. It is based on Chebyshev moments and has been proven to robust to the noise and image intensity [8].

The set of Chebyshev moments is based on the discrete Chebyshev polynomials. The nth-order N-point Chebyshev polynomial is def ned in recursive form as

$$t_n(x) = [(2n-1)(2x-N+1)t_{n-1}(x) - (n-1)(N^2-(n-1)^2)t_{n-2}(x)]/n \quad (3.4)$$

where $n = 2,3,\dots,N-1$ and $t_0(x) = 1$, $t_1(x) = 1 - N + 2x$.

The Chebyshev moment of order $(m+n)$ for an image $f(u,v)$ of size M × N, is given by

$$T_{mn} = \sum_{u=0}^{M-1}\sum_{v=0}^{N-1} \tilde{t}_m(u;M)\tilde{t}_n(y;N)f(u,v) \quad (3.5)$$

where $\tilde{t}_m(u;M)$, $\tilde{t}_n(v;N)$ are normalized Chebyshev polynomials.

It is simply the correlation between $\emptyset_{mn} = \tilde{t}_m(u;M)\tilde{t}_n(v;N)$ and the image ($f(u,v)$). Generally, the low-order Chebyshev moments capture the low-spatial-frequency components of an image, such as smooth surfaces which have a slow rate of variation in intensities. The high-order moments, on the other hand, capture those with high spatial frequency, such as edges and contours which have a high rate of variation in intensities. Based on this fact, the new focus measure is def ned as the ratio of the norm of the high-order moments to the norm of the low-order moments.

The low-order moments are taken to be the moments of order less than P. If the set of low- and high-order Chebyshev moments are denoted by Ł$(\tilde{f};P)$ and Ħ$(\tilde{f};P)$; respectively,

$$Ł(\tilde{f};P) = \{T_{kl} \backslash k + l \leq P\}, \tag{3.6}$$

$$H(\tilde{f};P) = \{T_{kl} \backslash k + l > P\}$$

And the Chebyshev focus measure of order P is defined as

$$M_T = \frac{\|H(\tilde{f};P)\|}{\|Ł(\tilde{f};P)\|} \tag{3.6}$$

Also from the Parseval theorem,

$$\|\tilde{f}\| = \|H(\tilde{f};P)\| + \|Ł(\tilde{f};P)\| \tag{3.7}$$

If the image $f(u,v)$ is normalized using Frobenius norm to $\tilde{f}(u,v)$ before finding the Chebyshev moments, Chebyshev focus measure (CFM) reduces to,

$$M_T = \frac{1 - \|Ł(\tilde{f};P)\|}{\|Ł(\tilde{f};P)\|} \tag{3.8}$$

This form, given in Eq. 3.8 is computationally much faster as only the Chebyshev moments with order less than P need to be evaluated.

To compare different FMs, a set of images were captured of the tip region, starting with Fig 3.8(a). A MP was slowly brought down towards the AFMC. When the contact occurs, the AFMC bends slightly as seen in Fig. 3.8(b). Three FMs were evaluated on these sets of images: CFM of order P = 7, CFM of order P = 14 and the Energy of Laplacian. The last one was selected as it has been shown to be the best of the

rest from Table 3.1. The results have been plotted in Fig. 3.9. The plot begins with MP at a height of 100 µm, Fig. 3.8(a). It is then gradually brought down towards AFMC. Contact occurs at around 28 µm, which causes the tip to bend, Fig. 3.8(b). The performance of the three FMs has been compared in Table 3.3. The judging criteria are:

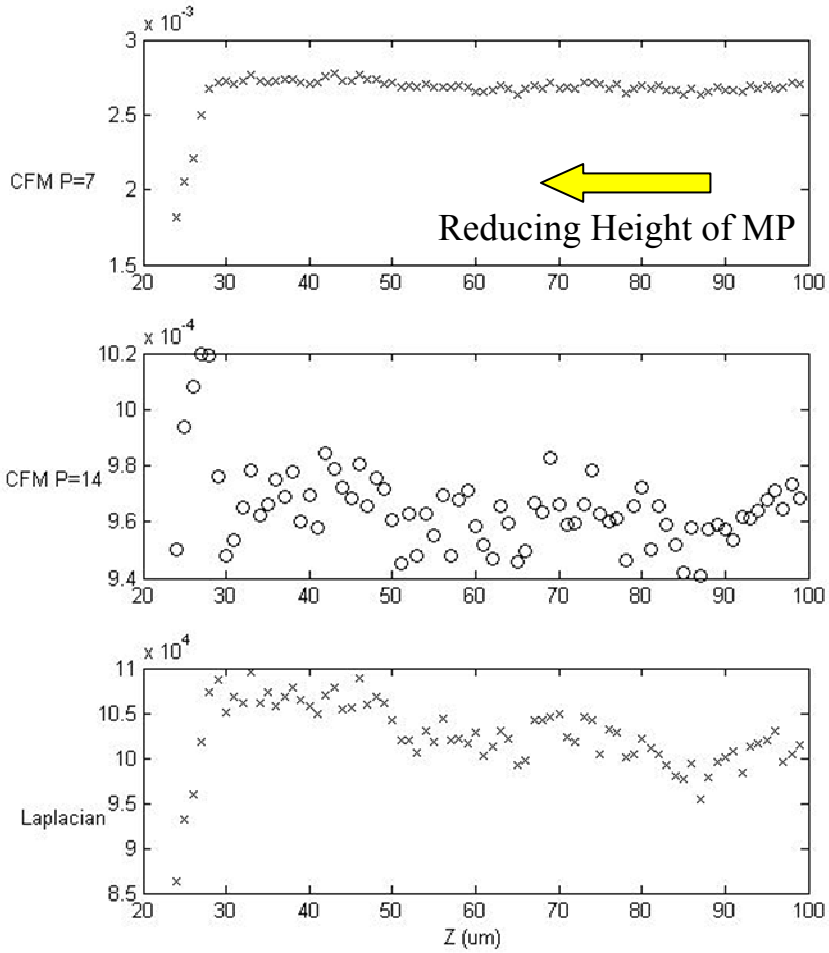

Figure 3.9 Different Focus Measures v height of MP. Height is gradually reduced until contact with AFMC occurs at around 28 µm.

- Standard deviation of the FM before the contact is made: Between the two heights (initial and contact) the scene remains almost the same. So the FM should also remain almost constant.
- The change in magnitude of the FM once the contact has been made: The greater the change the better the FM.
- Computational time

Table 3.3 Focus Measure Comparison for tip Bending

Focus Measure	Pre-contact σ / M_{avg} (%)	$\Delta M/M_{avg}$ (%)	Time (ms)
7^{th} order CFM	3.3	41	0.27
14^{th} order CFM	12.3	4	0.36
Energy of Laplacian	4.5	14	0.41

Although a higher order CFM is expected to be more sensitive to the blurring of the edges, it is also expected to be more sensitive to noise. This is shown in the higher pre-contact standard deviation of 14^{th} order CFM to the other two. 7^{th} order CFM is also the most sensitive to bending and requires the least amount of computational effort. Thus for tip bending detection 7^{th} order CFM is used.

3.4 Particle

Particle detection and tracking is required on multiple occasions in the entire process. In the particle pick-up step, the size of the particle has to be calculated to choose the one with the desired size. During the attachment step, its initial location has to be detected. The location is controlled afterwards as it is brought down towards the target location. It is also important to track the location of its reflection on AFMC.

3.4.1 Challenges

Apart from noise and background intensity robustness, the algorithm should achieve given accuracy consistently. The performance should not be compromised in the presence of any external objects. In the attachment step, the particle is held by the tip of MP. Sometimes the MP is visible with the similar intensity to that of the particle. In the particle pick-up step, a lot of time more than one particles are clustered side-by-side. This should not confuse the algorithm. It also has to perform when the image is blurred. As location of the particle is controlled during the attachment step, its depth is changed which takes it out-of-focus. Tracking should work under these circumstances too. Lastly a wide range of particle sizes are used for multi-axis AFM. The algorithm should be able to handle the entire range.

3.4.2 Particle Detection

Particle detection is only required in in-focus images. Hence out-of-blur is not a parameter. The in-focus images almost always have a decent contrast. The particle

appears as a dark blob in the image. The particle detection algorithm is divided into two parts: coarse detection and fine detection. The coarse detector finds the size and location of the particle with an accuracy of one pixel. While the fine detector searches for the best fit in the neighborhood of those parameters. The complete algorithm is shown in block diagram form in Fig. 3.10. The first two blocks belong to coarse detector. The robustness of this algorithm will be demonstrated on the image shown in Fig 3.3. The particle is held by a very dark tip of MP, which not very small as compared to the particle's size.

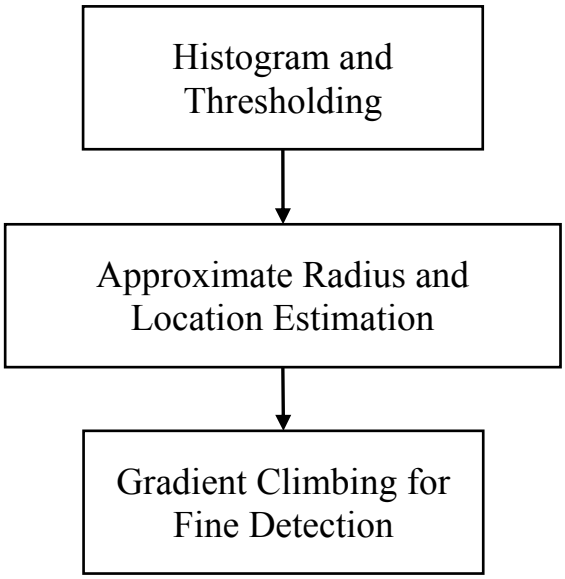

Figure 3.10 Block Diagram for Particle Detection Algorithm

A histogram of the image is created, as shown in Fig. 3.11. The bin size is kept large to minimize the effect of small variations throughout the image. As the particle is the darkest object in the scene, the peak with lowest intensity gives an indication of its

intensity. From Fig. 3.11 the particle's intensity can be set at 35. This threshold is used to mask the image, and all the pixels darker than the threshold are located. This forms the core of the particle. The centroid of these masked pixels is found and used as an initial approximation of the particle's center. Also the minimum diameter of the particle is

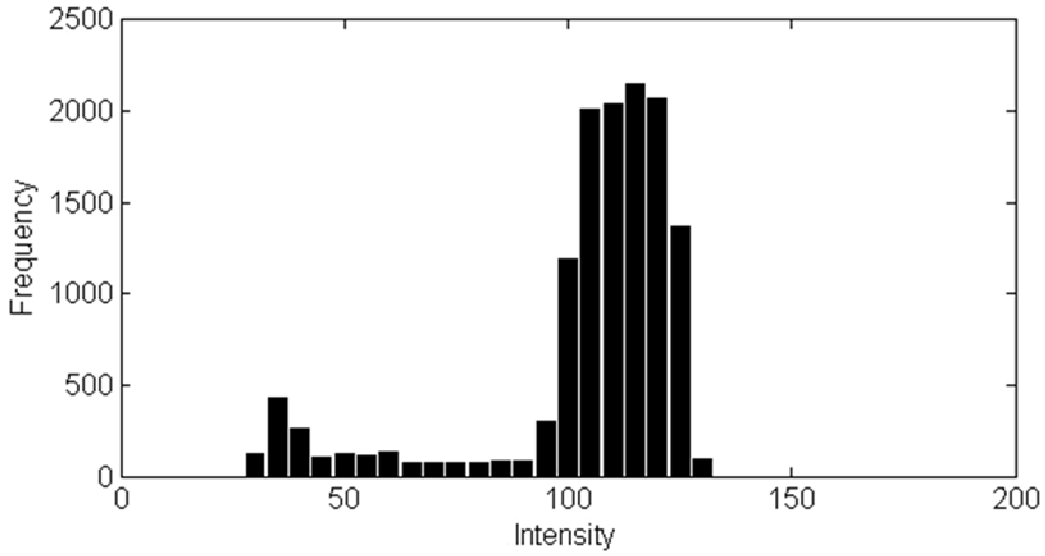

Figure 3.11 Histogram of image in Fig. 3.3 with a bin size of 5 grey levels

approximated to be the maximum width of this blob of masked pixels.

The coarse detector then searches at pixel-level in the vicinity of the initial approximation using correlation measure. The solution space is now three-dimensional: center location in the image and radius of the particle. Gradient based correlation is used, from Eq. 3.1, as it has been observed to perform better than the traditional intensity based

correlation in the presence of interfering objects and when the size of particle is unknown. If the center of the template is (u_0, v_0), the template is given by

$$g(u,v) = e^{-\frac{(d-r_0)^2}{2\sigma^2}} \tag{3.9}$$

$$d = \sqrt{(u-u_0)^2 + 4(v-v_0)^2}$$

Eq. 3.9 models the Gaussian blur with the standard deviation σ defined such that it is slightly larger than the resolving power of the microscope lens system.

The fine detector has the approximate location and size of particle, accurate to pixel level, as its input. As the exact size to the desired accuracy is still unknown, the gradient climbing approach is used. The result is the exact solution for the given problem. The result is shown in Fig. 3.12. A region is automatically defined which is used to track its movement in the latter stages.

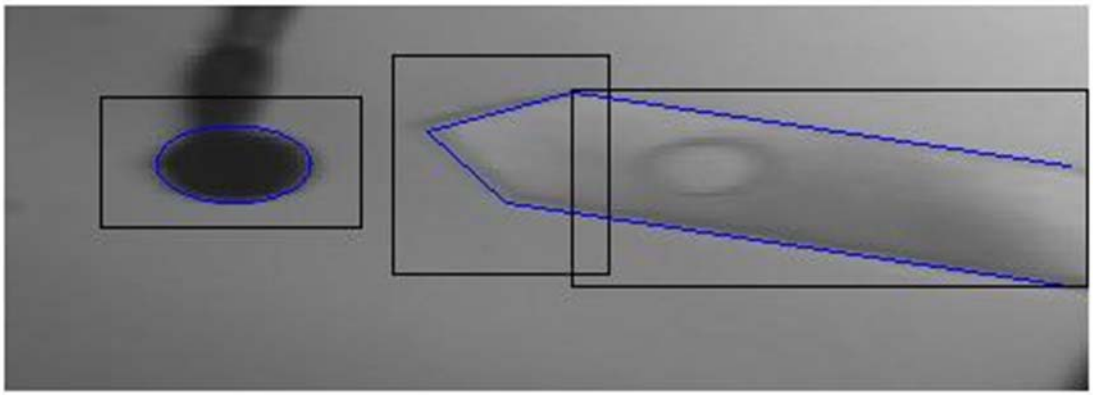

Figure 3.12 Final result of Particle and AFM detection algorithms

3.4.3 Particle Tracking

This algorithm tracks the change in location of the particle when it is actuated. It is an important component of the visual feedback that runs during the attachment step. The algorithm is required to perform when the particle is being manipulated away from the focal plane, which causes out-of-focus blur. This blur is taken into account when designing the template which is generally chosen conservatively. This template can in fact work for a wide range of depths of the particle.

The solution space is only two-dimensional, as the size of the particle is already known. A template can now be pre-generated with the desired accuracy. The default accuracy is 0.1 pixels which equals 0.67 μm in the RWCS. The template is generated at a higher resolution and downsampled before correlating with image.

A simple neighborhood search approach is used. The nomenclature used for the location of the particle in the solution space is shown in Fig. 3.13(a). The distance between two adjacent points in this solution space is defined by the desired accuracy of the tracking algorithm. Point i and its Correlation Measure would now be referred as P_i and C_i respectively. The algorithm is followed is illustrated by the flowchart in Fig. 3.13(b). The search algorithm is designed to minimize the number of correlation measures that are evaluated.

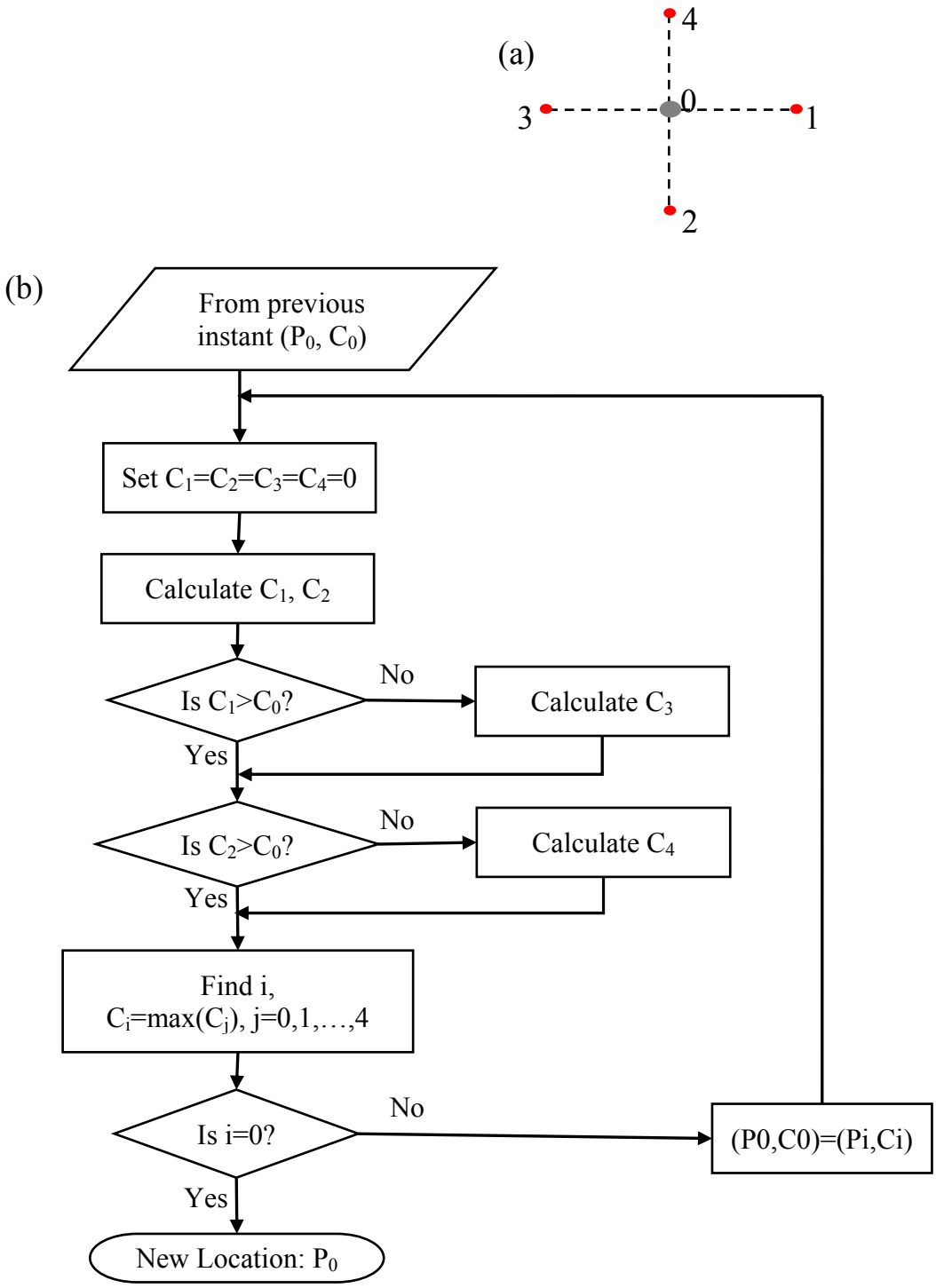

Figure 3.13 (a) Nomenclature of neighboring points in solution space (b) Neighborhood Search Approach

When all the neighboring C_i's are smaller than C_0, P_0 is declared to be the maxima, and hence the new location of the particle. If the starting location on the solution space is not very far off from the actual location, the correlation measure almost always has only one peak. This nullifies the chances of the search algorithm getting stuck in a local maximum.

This algorithm is sensitive to a background gradient pattern, especially when the particle is very blurred. When a high gradient background occurs, due to artifacts or the edge of another object, there is a possibility that it will remain stuck to the high gradient spot. In the attachment process, the only detectable external object is AFMC. Hence it is important to disregard any information obtained from pixels which are close to the edge of AFMC.

As the particle gets closer to AFMC, the separation between the particle and its reflection reduces. When the particle is very close, the two merge with each other, as shown in Fig. 3.14(b). In this scenario only the left half the particle pixels can be used to track its location. This reduces the amount of information available by half. There are chances of the tracking algorithm not being able to follow the particle perfectly. But the reduction in information only happens when the particle is close to AFMC and the focal plane, thus the information available is of higher quality. This, more often than not, compensates the dearth of data.

3.5 Reflection

Location of reflection, if present, gives an indication of the height of the particle from AFMC, as seen in Fig. 3.14. Knowing its location would also indicate when the two merge and tracking algorithms need to be altered to account for it. The reflection is always on the right side of the particle because of the stereo-angle of the microscope. Due

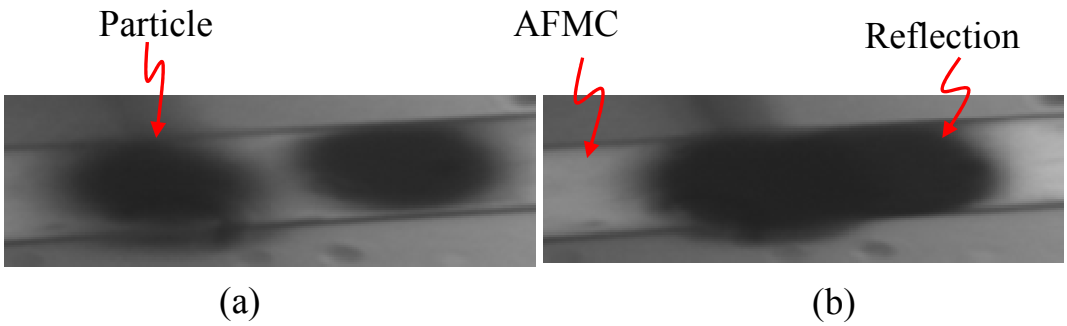

Figure 3.14 Reflection of the particle on the AFMC surface at two different particle heights

to this, the lower object always appears on the right even though the two may form same projection on the horizontal plane.

3.5.1 Validation

To validate that the second particle on the right is in fact the reflection and not its shadow, two tests were performed. In the first experiment, each of the three objects in the scene were focused one-by-one. The images thus captured are shown in Fig. 3.15. The reflection can clearly be seen in Fig. 3.15(c).

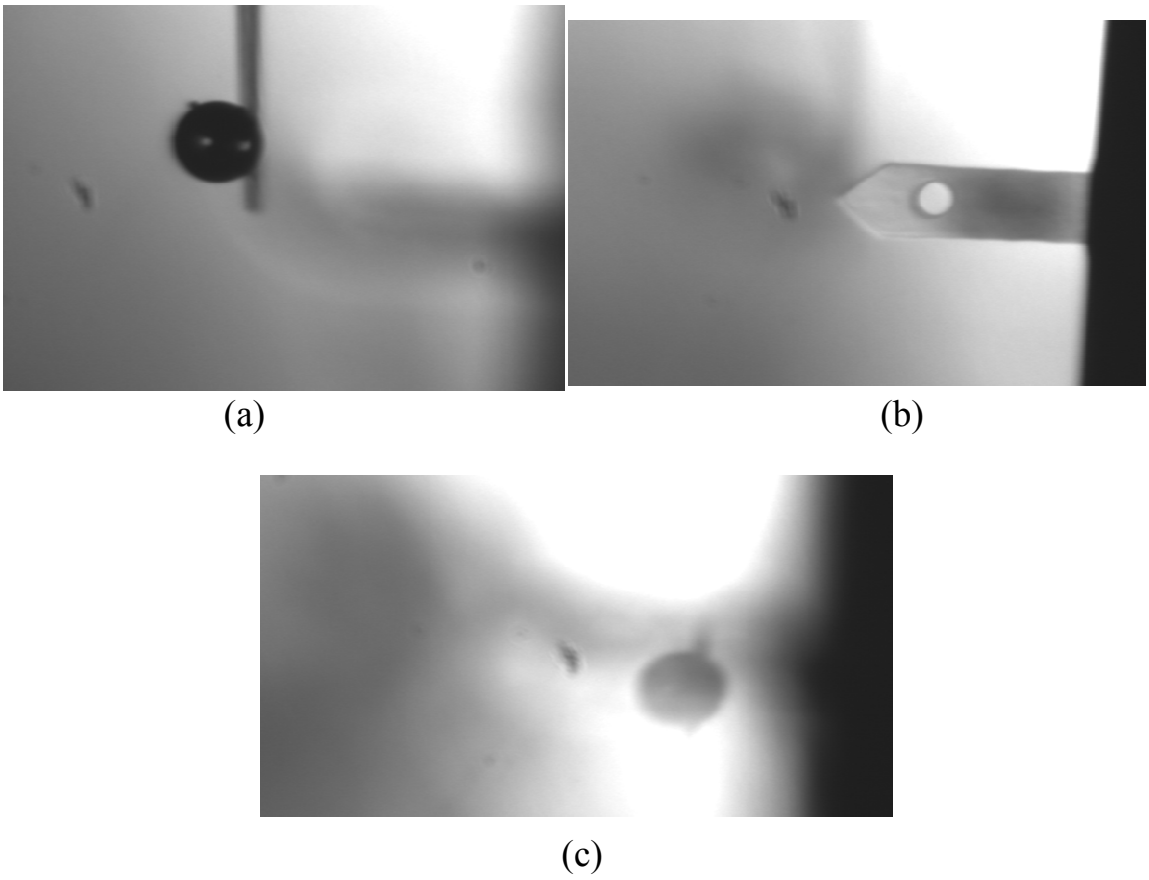

Figure 3.15 Particle is some distance above AFMC. The focus of microscope is shifted to (a) Particle (b) AFMC (c) Reflection

Another, more mathematical, test was performed for validation. First the particle and AFMC both were focused simultaneously implying that they were at same height. The particle was then moved manually using the screw gauges, to move it upwards. It was then hovered above the AFMC so that the second particle was visible. From the screw gauge readings: $\Delta z = 0.0059\, in = 149.9\, \mu m$. By knowing the separation

between the two particles (d), and the semi-stereo angle of the microscope (α), the height difference between the two was estimated:

$$\mathrm{d}\sin\alpha = 111.5 \text{ pixels} = 148.62\ \mu\mathrm{m}$$

$$d = 287.2\ \mu m$$

As the distance between the two particles is almost twice the distance between particle and AFMC, the second object has to be the reflection. Possible sources of error include the least count of screw gauge ($0.0001\ in = 2.54\ \mu m$) and that the AFMC not being perfectly horizontal.

3.5.2 Challenges

The main challenge of detecting and tracking the reflection is the lack of information. The only information that is available, lies is in the AFMC region. This could be very small for a particle of larger size. The data becomes even more limited when the particle and reflection merge. Only a part of the right edge remains useful. Since change in intensity is used for the detection of reflection, the vibration in the system could throw the algorithm off. Decently illuminated AFMC is required, to provide a larger change in intensity.

Nevertheless the two algorithms are aided by the knowledge of its size. Once the reflection has been located, tracking it is similar to tracking the particle. The same gradient template generated in Sec. 3.4.3 can be used on reflective region. Thus only its detection is described.

3.5.3 Reflection Detection

The simple fact, that as soon as the reflection becomes visible the AFMC region changes its intensity, is used to trigger its presence. Some robustness against vibration and illumination intensity change needs to be built into the triggers. The presence is triggered when:

1. A pixel in the AFMC region has intensity less than 60. This occurs when the reflection is visible, as it is always darker than this level. Although the edge of AFMC may also have similar intensity if oriented properly.
2. The same pixel from condition 1 shows an intensity difference of more than 90. It ensures that the pixel assumed to belong to reflection wasn't that dark to begin with. Even this could be triggered by vibration if AFMC region originally had widely varying intensity pattern.
3. The total intensity change in the AFMC region is more than 6000. It would be triggered if 60 pixels showed an intensity drop of 100. It ensures that the change is global and not just in a small region, which could be caused by noise. It is able to reject small vibrations for the same reason.

The first two conditions being less computationally intensive as compared to third, the third condition is only evaluated when they are satisfied. The algorithm is demonstrated by the images captured shown in Fig. 3.16. There are 12 pixels that satisfy the first two conditions, while third condition is satisfied by a huge margin of 6000.

The centroid of the light region in Fig. 3.16(c), weighted by the intensity difference, is used as the initial approximation of the location of this reflected particle.

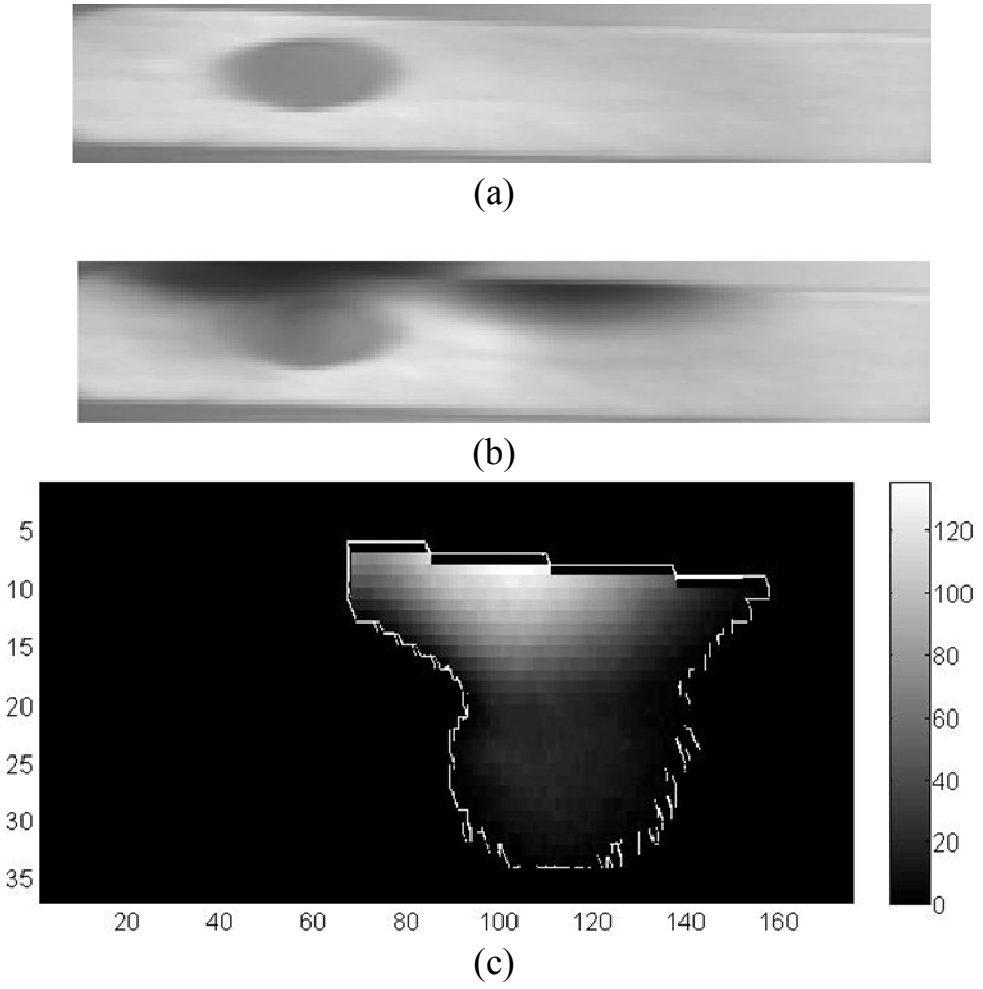

Figure 3.16 Reflective region of AFMC (a) Original (b) With reflection (c) Change of Intensity

The algorithm defined in Sec. 3.4.2 and Sec 3.4.3 for the detection and tracking of a regular particle are extended its detection and tracking as well. The only modification being that it will only correlate the template with the reflective region.

3.6 Micro-pipette

Micro-pipette is manipulated in the particle pick-up step and the glue dabbing step of the process. To be automated, the location of micro-pipette should be detectable. The image differencing approach similar to the one described in Sec. 3.4.2 will be used to detect the presence of MP. The scene is much cleaner in the glue dabbing step as the there are only two objects: MP and AFMC, while it can be much cluttered in the particle pick-up step. The mica sheet itself has a lot of artifacts, as can be seen in Fig. 3.17. Pixels with all the artifacts and any other low intensity external objects should be rejected. This reduces the amount of data available and disrupts the continuity.

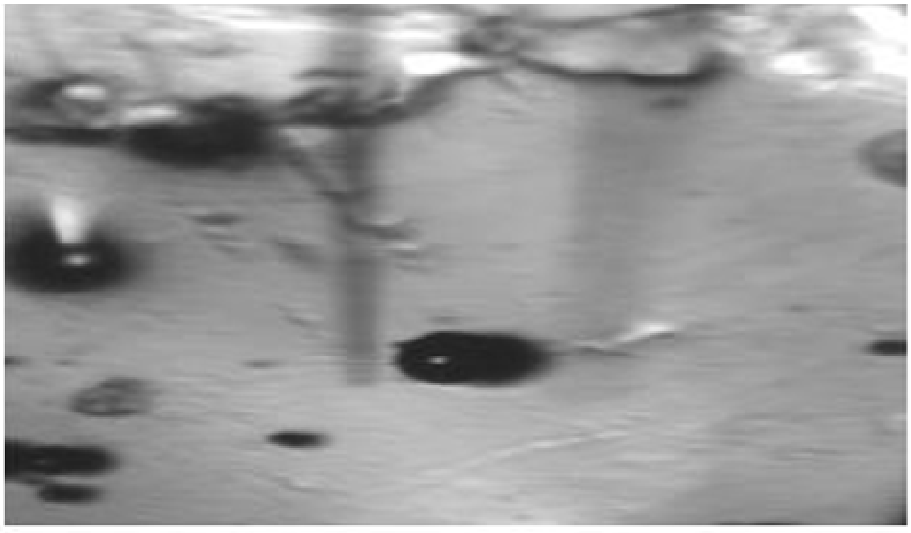

Figure 3.17 Starting Image for the Pick-up Step

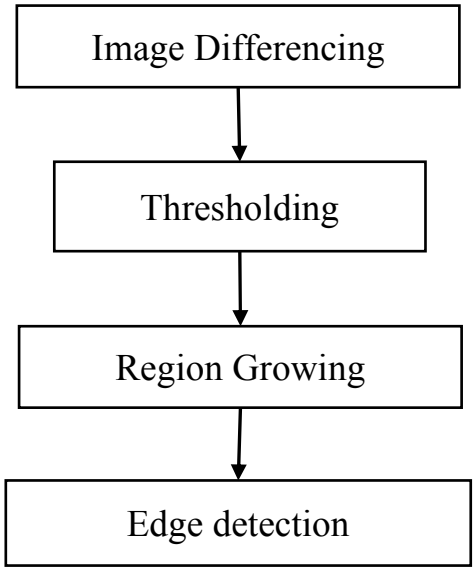

Figure 3.19 Block Diagram of Micro-Pipette Detection Algorithm

Various steps in the detection of MP are shown in Fig. 3.19. After the image differencing and Thresholding, the result obtained is plotted in Fig. 3.18. The two white

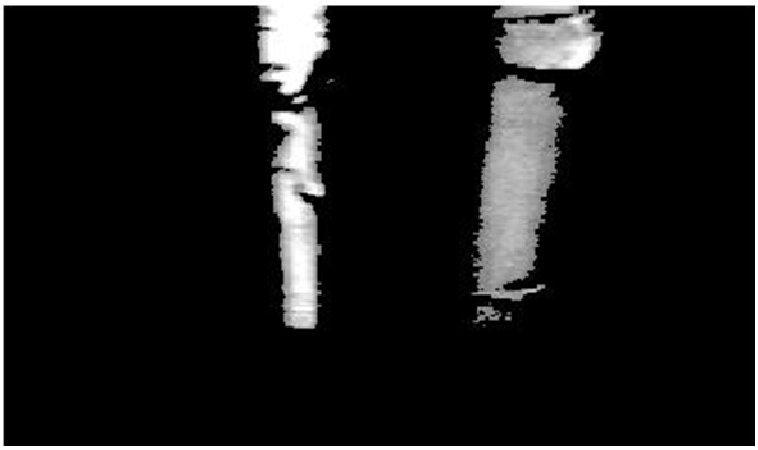

Figure 3.18 Post differencing and Thresholding

pin shaped objects are the MP and its reflection.

It is known that the MP always enters the image from the top edge. This fact is used in region growing to fill out various gaps in between two separate regions which should actually belong to a common region. The gaps are created due to the low intensity pixels which don't belong to MP. It is also known that MP is around 5 – 10 μm wide. This is used to distinguish between the particle and its reflection by calculating the horizontal separation between the two regions.

The next step is to find the edges of MP. All the pixels belonging to a region should lie on one side of the edge, as these definitely belong to the MP. The edge detection algorithm from Sec. 3.3.2 is used and the result obtained is shown in Fig. 3.20.

Since the edges have now been located, a template can be generated. The MP tracking algorithm uses the neighbor search approach, similar to particle tracking algorithm.

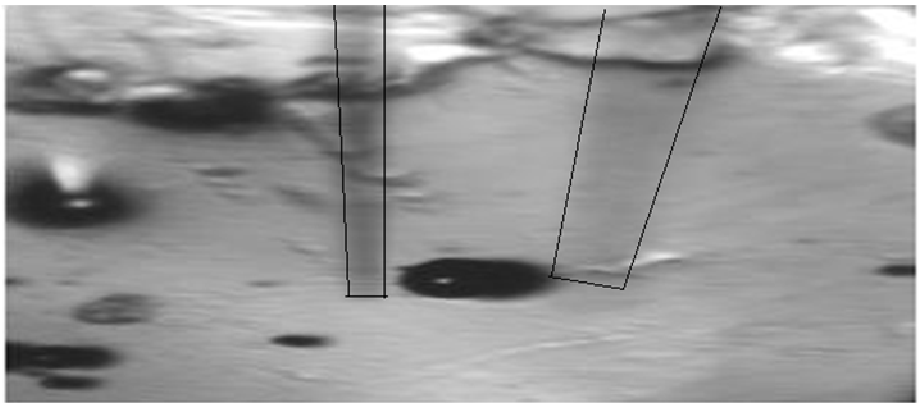

Figure 3.20 Detected MP

3.7 Summary

All the image processing algorithms used in this work have been described in this chapter. First the issue of vibration was dealt with by detecting the blur caused by the motion. Then the detection and tracking algorithms for each object was described. Different thresholds were set. The algorithms developed in this chapter will be used in the automated stages of the process described in next chapter.

CHAPTER 4

AUTOMATION

4.1 Introduction

As explained in Chapter 2, each step in the process has been divided in two stages: Manual and Automated. This chapter uses the setup designed in chapter 2 and the image processing algorithms developed in Chapter 3, to define the automated stage. Image location based position control approach is presented. All the components like the trajectory generator, controller etc. are described. The chapter concludes with a brief summary.

4.2 Control Strategy

The complete block diagram of the negative feedback control system is shown in Fig. 4.1. A desired trajectory is pre-generated. The lateral trajectory acts as the input to the control system. The feedback block operates on the images captured obtained from the images captured. It primarily computes the location of the objects in the image. The input to the controller is the difference in location of the object in image and its desired

location. The controller output is converted to the desired Nanocube location by an inverse model of the image formation process. The inverse actuator model then converts this location to the input voltage to the piezo-amplifier. The system includes everything

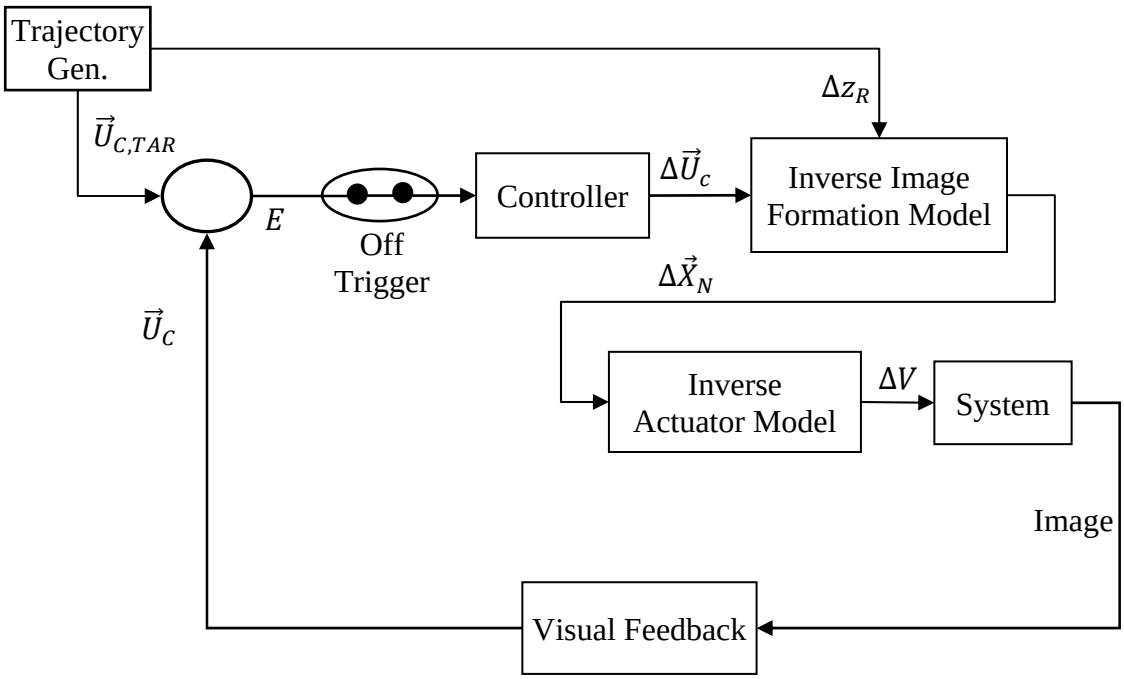

Figure 4.1 Bock Diagram of the feedback control system for the Automated stage

from Nanocube to the microscope and the camera. The change in the scene due to the new input is recorded by the camera and sent for visual feedback. The entire process is triggered off when a certain condition is met. This condition depends on the step which is being automated.

The object whose location needs to be controlled depends on the step being implemented. In the particle pick-up step, MP is manipulated. While in the glue dabbing

step, the drop of glue on MP is manipulated. In the attachment step, the particle at the tip of MP is manipulated. This is usually accommodated in the Visual Feedback part of the control process. The trajectory will also change. But the rest of the process pretty much remains the same.

The image processing algorithms used for visual feedback have already been described in Chapter 3. And the system used has been explained in Chapter 2. The rest of the blocks are described briefly in the next few sub-sections.

4.2.1 Controller

The input to the controller is the difference between the desired image location ($\vec{U}_{REF}$) and the actual location of the object ($\vec{U}_C$). A simple Proportional Controller with a gain of K_P has been found sufficient for this application.

$$\Delta\vec{U}_{C,E} = K_P\left(\vec{U}_{REF} - \vec{U}_C\right) \tag{4.1a}$$

The image processing algorithms cannot detect the displacement if the object moves out of a region. And it becomes even harder to track the object when the background itself has high gradient pattern. Thus the displacement is limited by a threshold ($\Delta U_{C,T}$).

$$\Delta U_{Ci} = \begin{cases} \Delta U_{C,Ei}, & \left|\Delta U_{C,Ei}\right| < \Delta U_{C,T} \\ \Delta\, U_{C,T}, & \left|\Delta U_{C,Ei}\right| \geq \Delta U_{C,T} \end{cases}, i = 1,2 \tag{4.1b}$$

4.2.2 Inverse Image Formation Model

An image formation model was derived in Sec. 2.5. The same equations have been used to derive the inverse model. The input to this block is the desired change in location in pixels ($\Delta\vec{U}_C$). This inverse model will return the corresponding change in Nanocube location ($\Delta\vec{X}_N$).

$$\Delta\vec{U}_M = \begin{bmatrix} cos\ \theta_1 & 2sin\theta_1 \\ -sin\theta_1 & 2cos\theta_1 \end{bmatrix} \Delta\vec{U}_C \tag{4.2}$$

$$\Delta x_R = \frac{1}{cos \propto}\left(\frac{c}{M}\Delta u_M + \Delta z_R sin \propto\right) \tag{4.3}$$

$$\Delta y_R = -\frac{c}{M}\Delta v_M$$

$$\Delta\vec{X}_N = \begin{bmatrix} -cos\theta_2 & sin\theta_2 & 0 \\ sin\theta_2 & cos\theta_2 & 0 \\ 0 & 0 & 1 \end{bmatrix} \Delta\vec{X}_R \tag{4.4}$$

The parameters have been defined in Sec. 2.5. Eqs. 4.2 – 4.4 provide the inverse model for the image formation process.

4.2.3 Actuator

The actuator is a three-axis piezo-electric motion stage called Nanocube. It is an open loop system. It is connected to the computer through an E-505 Position Servo-Control Module, as shown in Fig. 4.2. The input voltage range is 0 – 10.24 V.

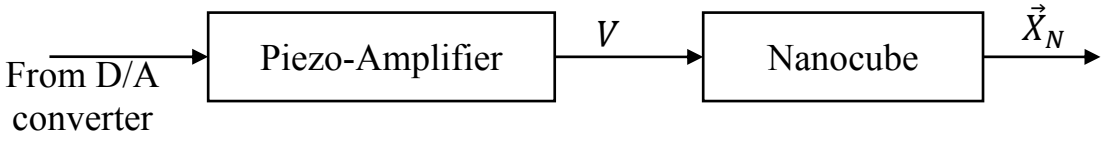

Figure 4.3 Actuator Block Diagram

According to the specifications provided by Physik Instrumente, the amplifier has a wide dynamic range. It is operated under open loop configuration. The frequency response of the entire actuator system in open loop has been plotted in Fig. 4.3. The static

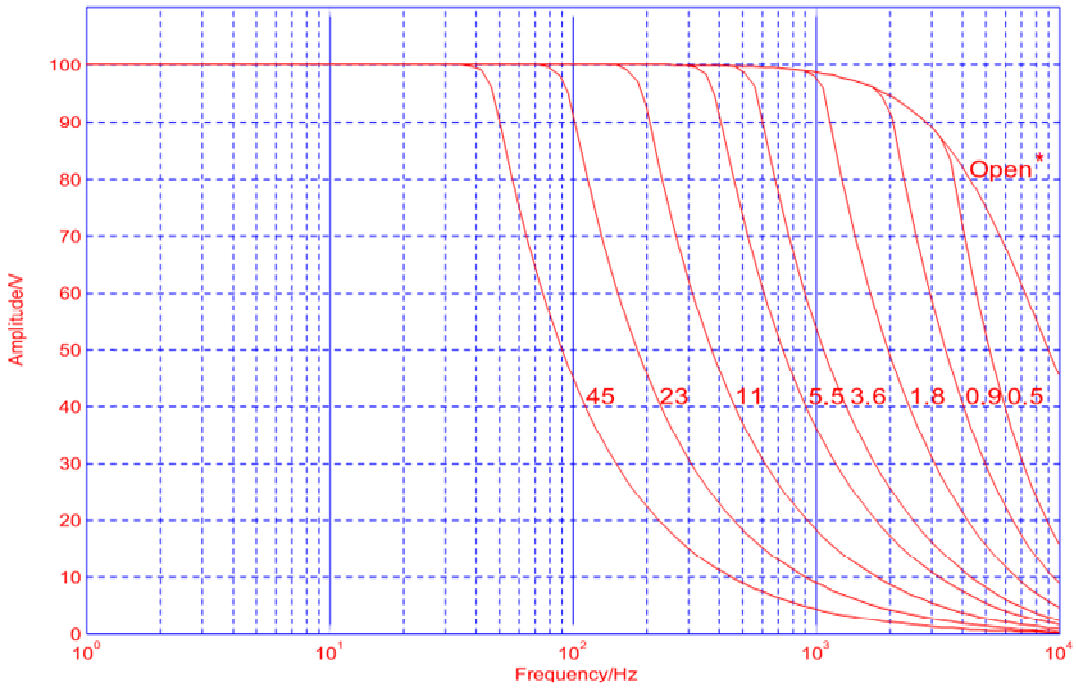

Figure 4.2 Frequency response of the actuator according to the manufacturer's specifications

gain is 10 μm/V. This control process uses an operating frequency of 10 – 100 Hz. For this frequency range, the response curve in open loop is flat and hence the actuator can be assumed to be a zero-order system

$$\vec{X}_N = 10\,\vec{V}_{IN} \tag{4.5}$$

$$\vec{V}_{IN} = [0,10]V$$

Since the piezo-transducers are known to display hysteresis and creep [9], it is necessary to examine this behavior before using Eq. 4.5 blindly. The input voltage to the Nanocube was varied such that it would move vertically. CFM was computed on the captured images of the particle which was kept on the Nanocube. The result obtained has

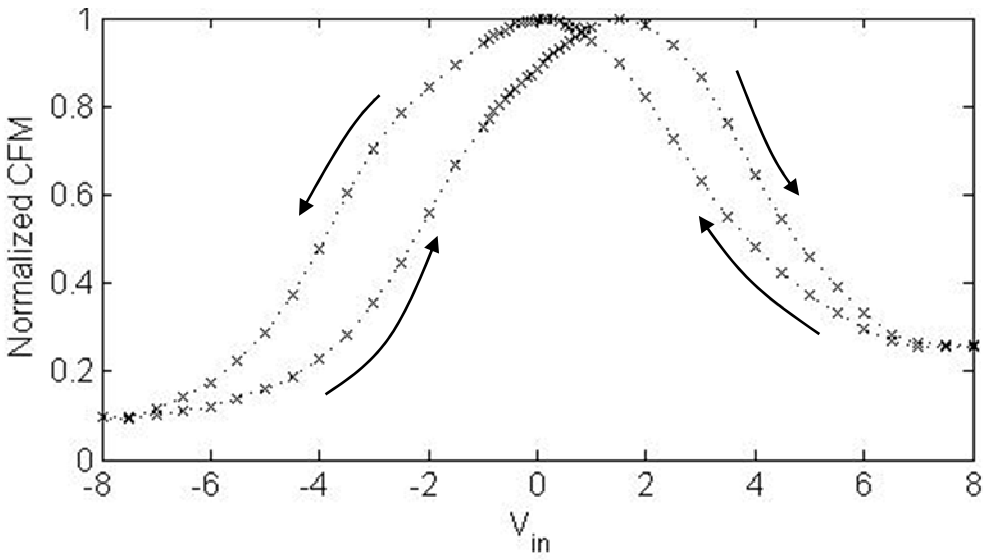

Figure 4.4 Blur Measure v Out-of-focus depth generated by Nanocube. Direction of motion has been pointed out.

been plotted in Fig. 4.4.

As the particle moves away from the focal plane, the CFM starts reducing. Although the exact mathematical relation between the distance from focal plane (d) and CFM has not been evaluated, the CFM is expected to decrease monotonously with d. Additionally two points with the same CFM that lie on the same side of focal plane, will have same d. As can be seen from Fig. 4.4, the peak occurs at different input voltage when travelling in different direction. Same holds true for other points of same height. The two peaks are off by about 2V, which is a considerable amount of hysteresis.

4.2.4 Trajectory Generator

The starting point of an attachment step is shown in Fig. 4.5. The particle is brought manually to within the motion range of Nanocube. And it is approximately level

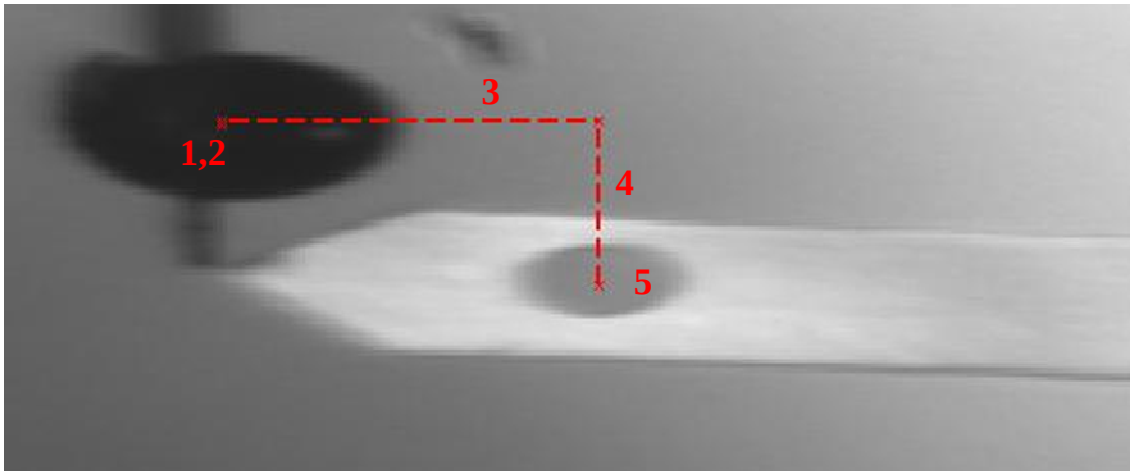

Figure 4.5 Generated Lateral Trajectory, Phases 1 - 5

with the AFMC. This is ensured by focusing on particle, as AFMC already lies in focal plane. Since the approach used controls the location in the image, the lateral positions are generated in image pixels. The vertical dimension is still generated in the RWCS.

The goal is to bring the particle around the AFMC and gradually lower it to the target location. The trajectory is divided in different phases. These have been marked in Fig. 4.5.

Phase 1 involves raising the particle by sufficient amount so that it can be safely brought on top of AFMC without touching it. Since the actuator has some inherent hysteresis, it is important to include a safety factor to ensure that no contact is made prior to the final step. If the safety factor is too high, the particle would be moved further away from the focal plane. It may get so blurred that the tracking algorithm is unable to follow the particle. A safety factor of 1.8 was found to consistently give just the right amount of gap between the particle and AFMC, without too much of blur. Since the vertical motion range of Nanocube is only 100 μm, the maximum sized particle that can be attached without compromising the safety factor is 56 μm. This can be extended by using a motion actuator with a higher range.

The lateral position, in pixels, is kept the same. Phase 2 moves the particle sufficiently away from AFMC, so that its edges don't affect the particle tracking. In Fig. 4.5, these two locations happen to be very close to each other. Phase 3 and 4 bring the particle on top of the target location such that it crosses the AFMC along the side edge. Vertical height is kept constant until this Phase 5.

Phase 5 involves gradually bringing down the particle to its target location, while its lateral position is held constant. This is the final phase of the attachment step.

4.2.5 Off Trigger

Once the particle makes contact with the AFMC, any more downward movement of the MP would result in slight bending of AFMC. The deflection would be maximum at the tip of AFMC. As described in Sec. 3.2.3, the tip deflection is best detected by a Chebyshev Focus Measure of order 6. Since the FMs were tested on an image and AFMC tip of similar size to the ones in actual process, the spatial frequency content should remain about the same. Hence the order 6 would suffice this trigger.

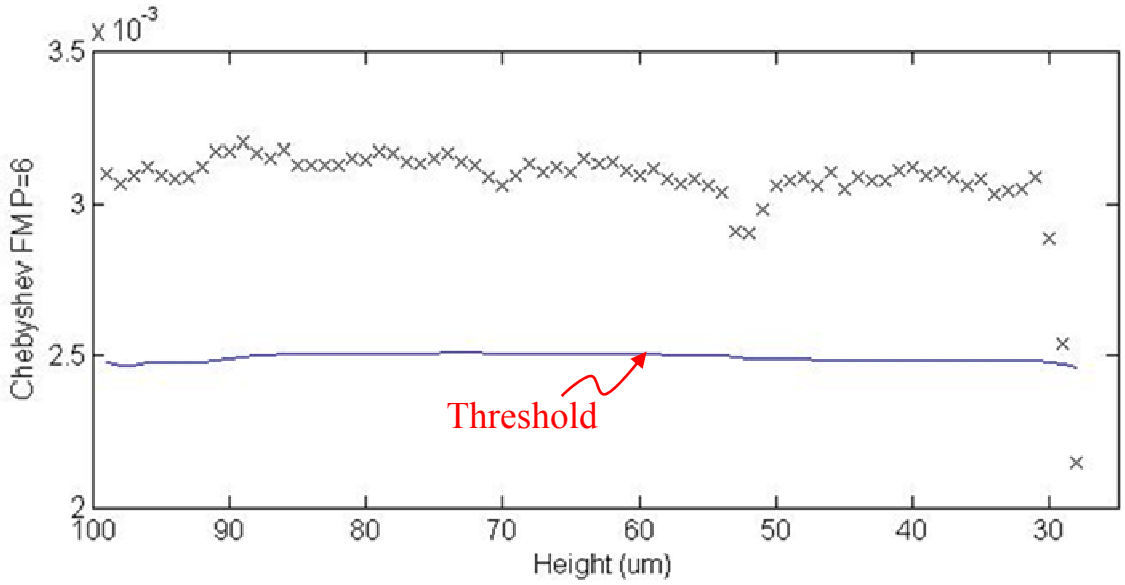

Figure 4.6 Chebyshev FM of order 6 and the threshold as the particle is brought down and in contact with AFMC

When the contact occurs, the tip would move out-of-focus or in-focus depending on the initial tip location with respect to the focal plane. Thus the CFM could increase or decrease. The trigger goes off when the CFM changes more than 20% of the average value, as shown in Fig. 4.6. Thus the upper threshold is set at 120%, while the lower adaptive threshold is set at 80% of average of CFM of all the previous samples. A threshold higher than 80% was observed to give false triggers. On the other hand, if it was lower than 80%, AFMC would have to be bent by a larger amount for the trigger to go off. This increases the risk of damage to the AFMC. Within 3 μm of deflection, the 80% threshold is crossed and the process is triggered off.

The control approach presented here can be used in particle pick-up, glue dabbing step in addition to the attachment step. Only the image processing and trajectory generator need to be switched for the shape to be identified and controlled.

4.2.6 Parallax Error

The control approach presented in this section controls the position on the image. This sometimes may not provide the desired accuracy. The reason is that the scene is viewed at the semi-stereo angle. Similar to the parallax error in measurement, even though the particle may appear to be attached at the target location, it will always be slightly off, as shown in Fig. 4.7.

The error in the particle location would be:

$$E_P = r\ tan \propto \tag{4.6}$$

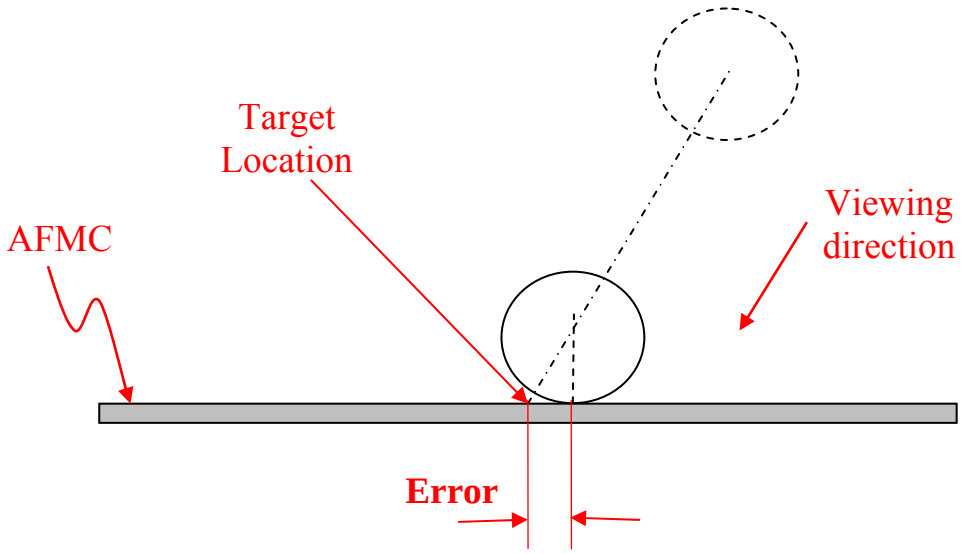

Figure 4.7 Error in Particle Attachment due to semi-stereo angle

This error increases as the particle size increases. It might become unacceptable if the particle size is large. An alternate approach would be required to bring down the particle vertically. This would require the knowledge of the particle height. And only one image is available to extract this information. Out-focus depth can be estimated by finding the blur. But it the optical blur modeling is very involved even for a single lens system [10].

One way to reduce this error is to shift the target location to account for the error E_P. The corresponding $\Delta\vec{U}_{C,sh}$ shift in the image is given by:

$$\Delta\vec{U}_{M,sh} = \begin{bmatrix} \frac{M}{c} E_P \cos \propto \\ 0 \end{bmatrix}$$

$$\Delta\vec{U}_{C,sh} = \frac{M}{c} E_P \cos \propto \begin{bmatrix} cos\theta_1 \\ 1/2 \, sin\theta_1 \end{bmatrix} \tag{4.7}$$

A hole is sometimes machined on the target location of the AFMC. This helps better hold the particle in its place during experimentation. The hole is obviously of a smaller size than the particle. In this case the particle settles down in the center of this hole, even if it is not dropped exactly at the target location. Hence the parallax error is not a problem when a hole has been machined at the target location.

4.3 Summary

This chapter describes the Visual Feedback Control System for all the steps to be automated. Location of the object in the image is controlled using a Proportional Controller. Other components like the trajectory generator and the actuator are described. A main source of error is presented and potential solutions are considered. The results of the calibration and the control process will be presented next.

CHAPTER 5

RESULTS

5.1 Introduction

All the results obtained are presented in this chapter. It begins with a description of calibration of various system parameters that remain constant during the experiment. Next a few validations of the concepts presented earlier are described. Control strategy results are presented next, with a description of the choice of control parameters. And the chapter ends with a brief summary.

5.2 Calibration

The geometric parameters that remain constant can be calibrated before the experiment. Three such parameters deal with the relative orientations of the different components in the setup. These are required during the real-time operation. Their calibration is explained in the next few subsections.

5.2.1 α Calibration

As described earlier in Sec. 2.5, α is the semi-stereo angle of the microscope. It is a property of the microscope and remains constant in all the experiments. Thus it only needs to be calibrated once.

The semi-stereo angle causes the image of the object to move even when it is only displaced vertically. This property is used for its calibration. If a vertical displacement (Δz_C) is produced, keeping the lateral position constant, the corresponding change in the image location can be measured. From Eqs. 2.4 – 2.6,

$$\Delta\vec{U}_M = \frac{M}{c}\begin{bmatrix} -sin\,\alpha \\ 0 \end{bmatrix}\Delta z_C$$

$$\Delta\vec{U}_C = \frac{M}{c}\begin{bmatrix} cos\theta_1 \\ \frac{1}{2}sin\theta_1 \end{bmatrix}(-\Delta z_C sin\propto) \tag{5.1}$$

$$sin\propto = \frac{c}{M}\frac{\sqrt{\Delta u_C^2 + 4\Delta v_C^2}}{\Delta z_C} = \frac{c\Delta p}{M\Delta z_C}$$

It is rewritten in the following form to use the least square fit when more than one data points are available:

$$sin\propto = \frac{c}{M}\frac{\sum_i \Delta p_i \Delta z_{Ci}}{\sum_i \Delta z_{Ci}^2} \tag{5.2}$$

The main hurdle in this calibration is to accurately generate the vertical displacement. Nanocube cannot accurate displacements as it is an open loop system with

considerable hysteresis. The screw gauge for the vertical axis on the manual motion stage is used for this purpose. The resolution is only $0.0001\ in\ =\ 2.54\ \mu m$, which makes it difficult to produce small displacements. If the displacement is too large, the accurate position detection becomes difficult, as the image gets very blurred.

The experiment was repeated a number of times within a small range of vertical displacements. The screw gauge was turned in one direction only to eliminate the effect of play. The results obtained and the least square fit is shown in Fig. 5.1.

After calibration α was found to be 15.3°.

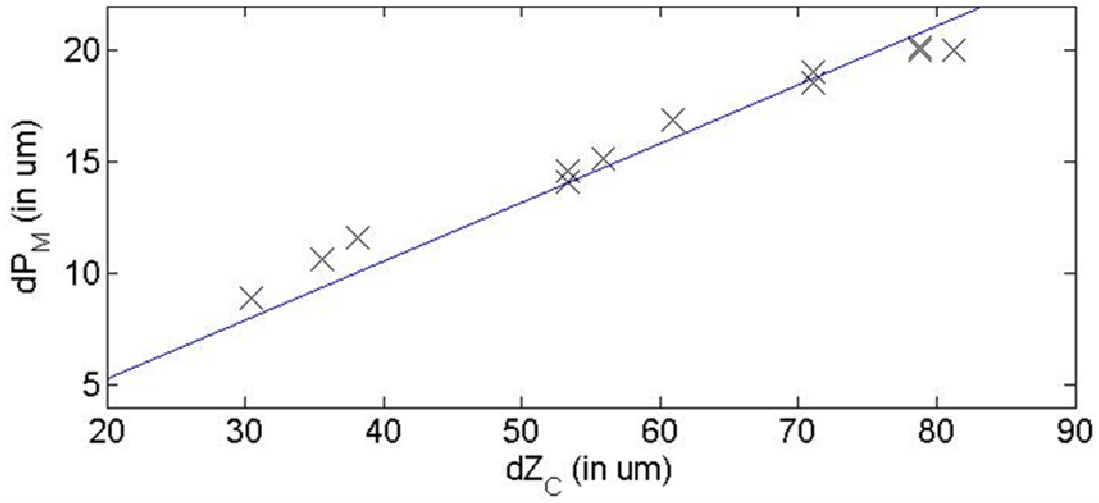

Figure 5.1 α calibration data and least square fit

5.2.2 θ_1 Calibration

As described in Sec. 2.5, θ_1 defines the orientation between the camera and the microscope. It is caused by the wear and tear in the threads in the camera adapter. This orientation could change between experiments due to the wear or the looseness if the fit. Hence it is important to calibrate this parameter before every experiment.

The particle is actuated in the vertical direction keeping the lateral position constant. Due to the semi-stereo angle, the displacement should ideally occur along the u_C axis in the image. The actual direction of the displacement in the image is measured

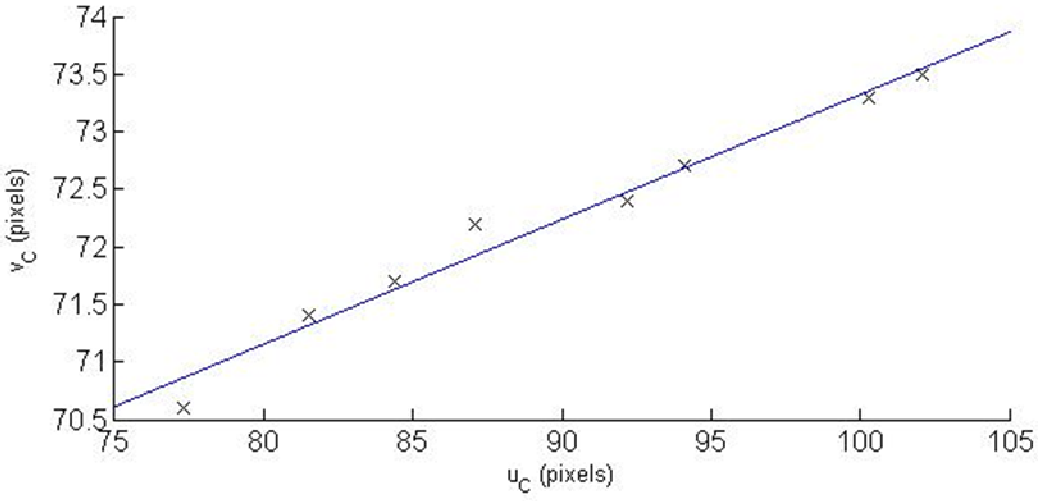

Figure 5.2 θ_1 calibration and least square fit

which leads to θ_1.

$$\Delta v_M = 0 \Rightarrow -\Delta u_C \sin\theta_1 + 2\Delta v_C \cos\theta_1 = 0 \tag{5.3}$$

The least square fit can be defined as:

$$[u_{Ci} \quad 1]\begin{bmatrix}\tan\theta_1 \\ c\end{bmatrix} = [2v_{Ci}] \Rightarrow Ax = b$$

$$\begin{bmatrix}\tan\theta_1 \\ c\end{bmatrix} = (A'A)^{-1}A'b \tag{5.4}$$

where (u_{Ci}, v_{Ci}) is the location of the particle in the image. The calibration data for one of the experiments has been plotted in Fig. 5.2. The comparatively large standard deviation is caused by the vibration, which causes a slight error in the position of the particle. θ_1 is calibrated to 12.3°.

5.2.3 θ_2 Calibration

As described in Sec. 2.5, θ_2 defines the orientation between the Nanocube axes and the RWCS which is aligned with the microscope. This is usually performed after θ_1 calibration since it must be known for this calibration. The particle is displaced along x_N axis, this causes its image to displace along θ_3 direction, which is determined by least squares to reduce the effect of vibrational noise in the measurement.

$$[u_{Ci} \quad 1]\begin{bmatrix}\tan\theta_3 \\ c\end{bmatrix} = [2v_{Ci}] \Rightarrow Ax = b$$

$$\begin{bmatrix}\tan\theta_3 \\ c\end{bmatrix} = (A'A)^{-1}A'b \tag{5.5}$$

It can be shown from Eqs. 2.4 – 2.6,

$$\Delta y_N = 0 \Rightarrow \tan\theta_2 = \tan(\theta_3 - \theta_1)\cos\propto \tag{5.6}$$

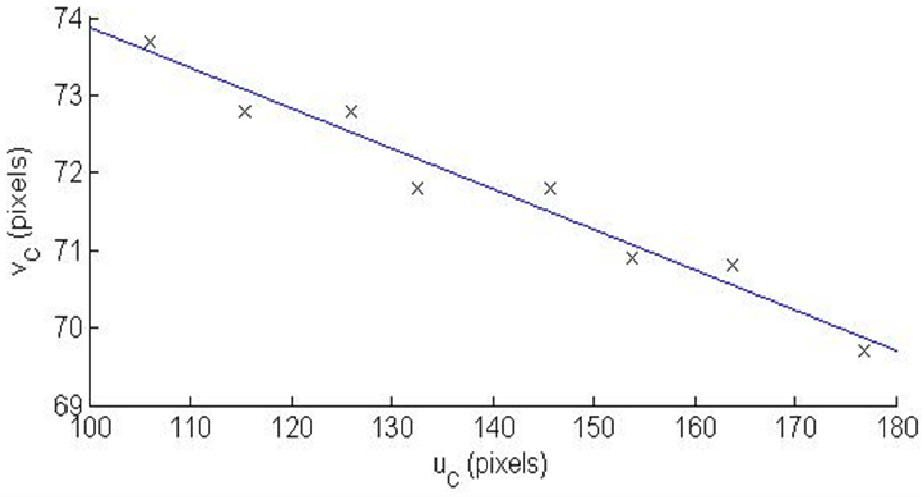

Figure 5.3 θ_2 calibration data and least square fit

The calibration data and the least square fit obtained are shown in Fig. 5.3. θ_2 was calibrated to -17.4°.

5.3 Control Strategy

The control strategy presented in Sec. 4.2 has been implemented for the attachment step and the results are described next in two parts. First the effect of the control parameters: Controller gain (K_P) and the displacement threshold ($\Delta U_{C,T}$), is observed. Then the results from the attachment step with the chosen control parameters implemented are presented.

5.3.1 Control Parameters

The particle has to be typically displaced by almost the whole range of motion provided by piezo-actuator to reduce the manual involvement. This implies that the particle is about 100 pixels away from the target location when the control process has just begun. But the threshold is kept low to reduce the chances of the tracking algorithm losing the particle. Hence even though the error ($\vec{U}_{REF} - \vec{U}_C$) is large, the control

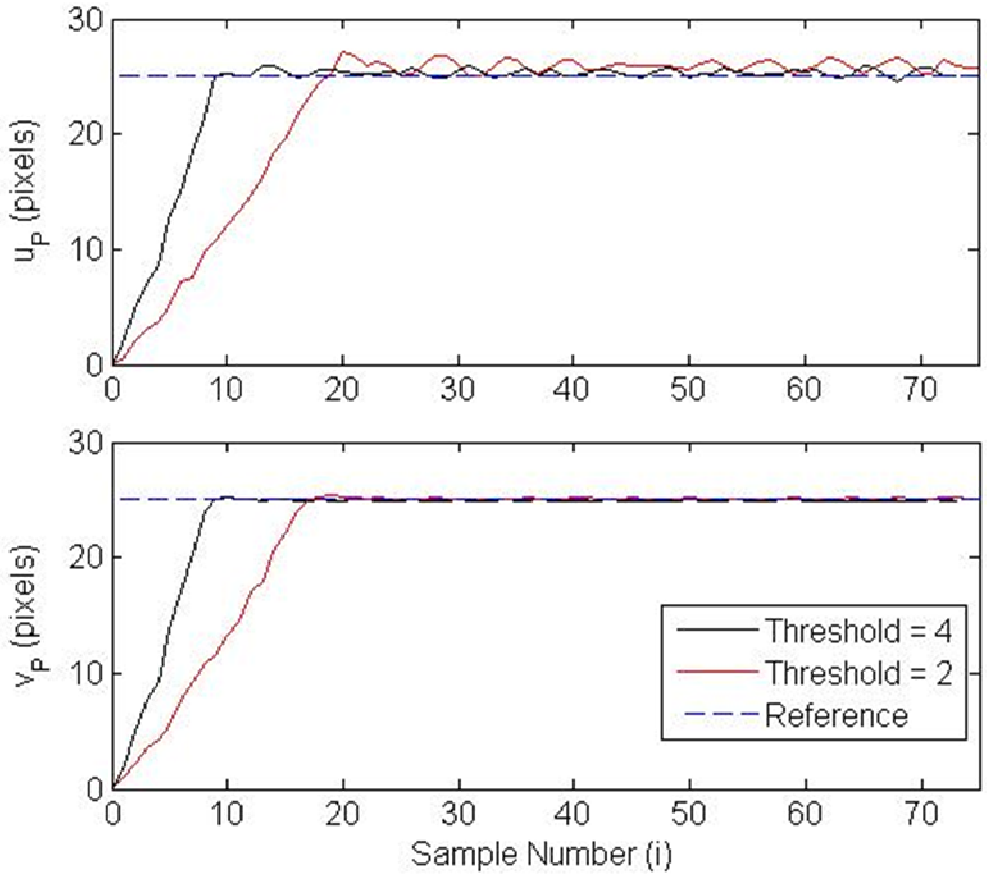

Figure 5.4 Effect of threshold on System Response. Controller gain was kept constant.

action is kept low because of the threshold ($\Delta U_{C,T}$). Hence the initial response is dictated by the threshold and not the controller gain. As can be seen in Fig. 5.4, the rise time is almost doubled when the threshold is reduced by half. After several more experiments threshold was set at 4 pixels. It is not too fast so that tracking algorithm can work under varying circumstances, and not too low so that it provides fast enough rise time.

After the particle moves within the threshold range, the response is dictated by the

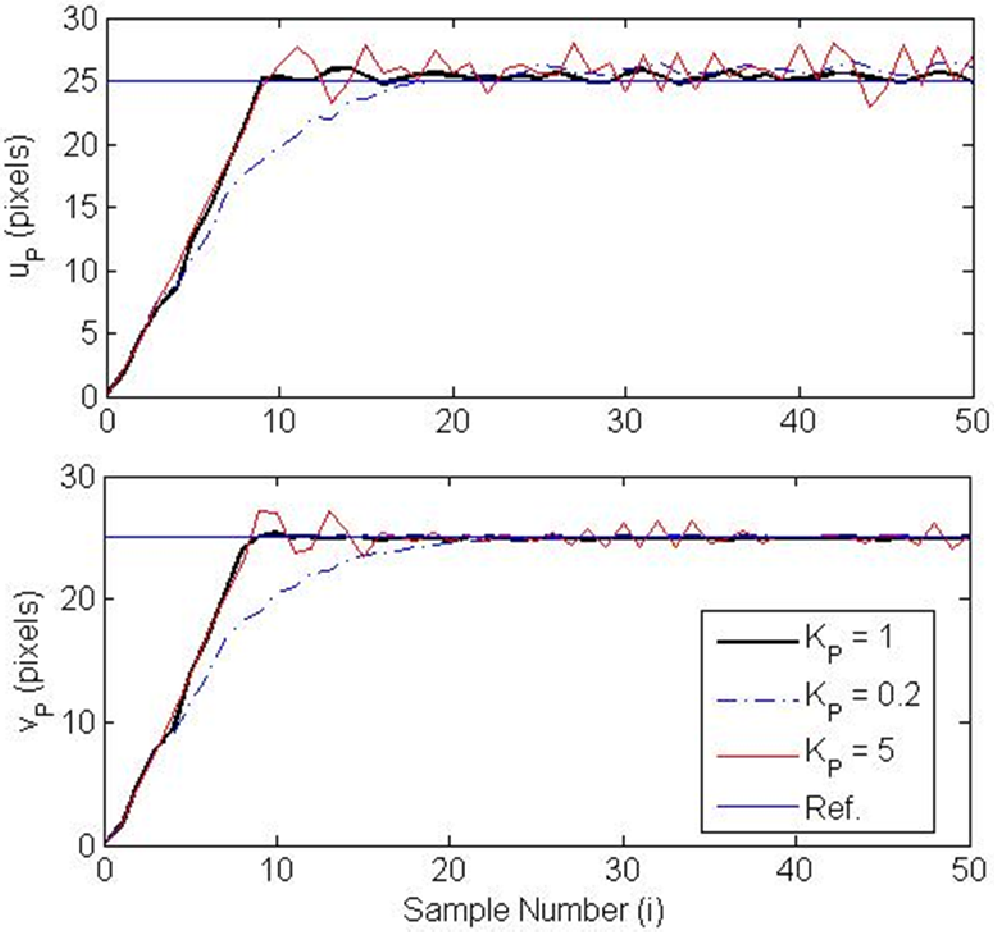

Figure 5.5 Effect of K_P on system response

controller gain (K_P). Three controllers were tried with different gains. The result has been plotted in Fig. 5.5. Gain of 5 is too high as it causes system to overshoot and is very sensitive to the vibration. On the other hand a gain of 0.2 is too low as it slows the response down. On the positive side it compensates for the vibration very well and shows no overshoot. The gain of 1 is just right with not much overshoot, fast response and good vibration compensation. Thus the controller gain was set at 1.

The controller parameters designed here is used in the automation stage. And the

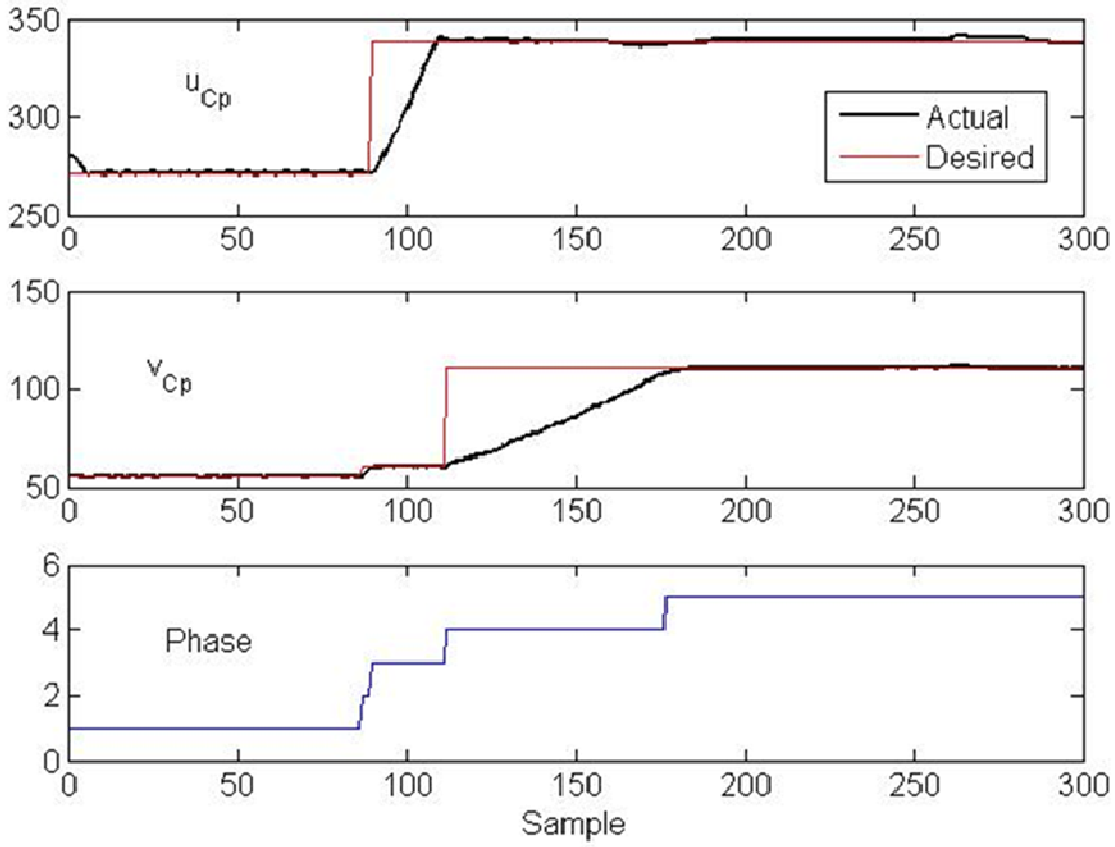

Figure 5.6 System response during the attachment step

results are described in the next section.

5.3.2 Attachment Step

The control system developed is demonstrated on the attachment step. Other steps use a slightly modified system to accommodate for different conditions, but the performance remains similar.

The system response is the location of the particle in the image. It has been plotted for the entire step in Fig. 5.6. The desired location changes as the process trajectory generator updates the phase whenever previous target is acquired.

The control output is displayed in the form of the desired change in Nanocube

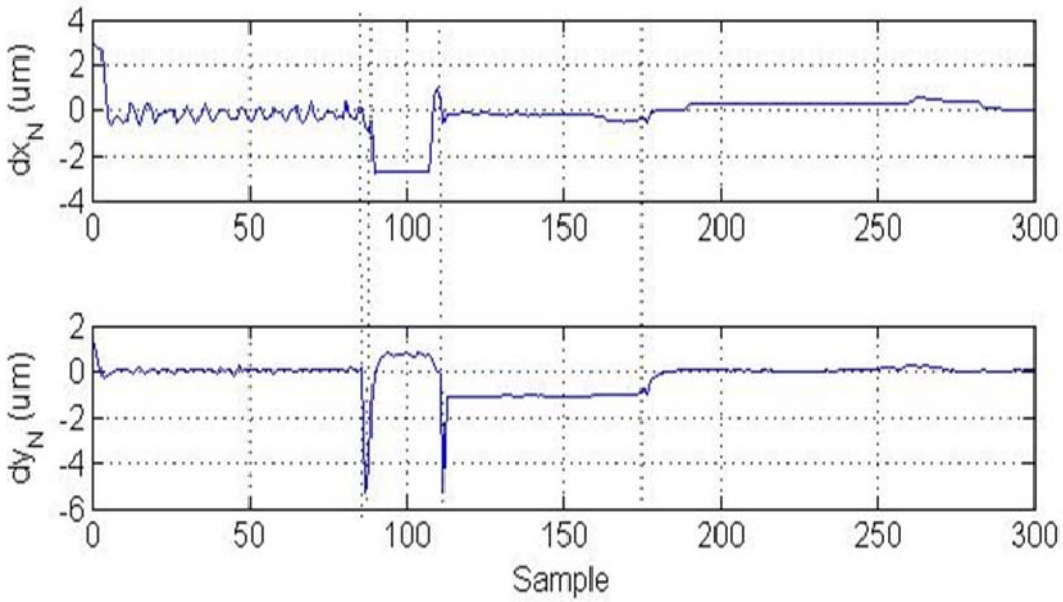

Figure 5.7 Modified Control Output

location. This is obtained after manipulating the actual control output with the inverse system model. This has been plotted in Fig. 5.7. The dotted lines show the change in phase of the trajectory generator. The control output spikes after every change in phase. In phase 1, the particle is brought up. The control output continuously compensates for the shift that causes in the image, through the semi-stereo angle of the microscope. The same behavior can be seen in phase 5 when the particle is being brought down to its target location. In rest of the phases particle is only displaced laterally. The phase changes and their corresponding target locations have been plotted in Fig. 4.5.

The last important variable is the CFM. Its variation is shown in Fig. 5.8. It is

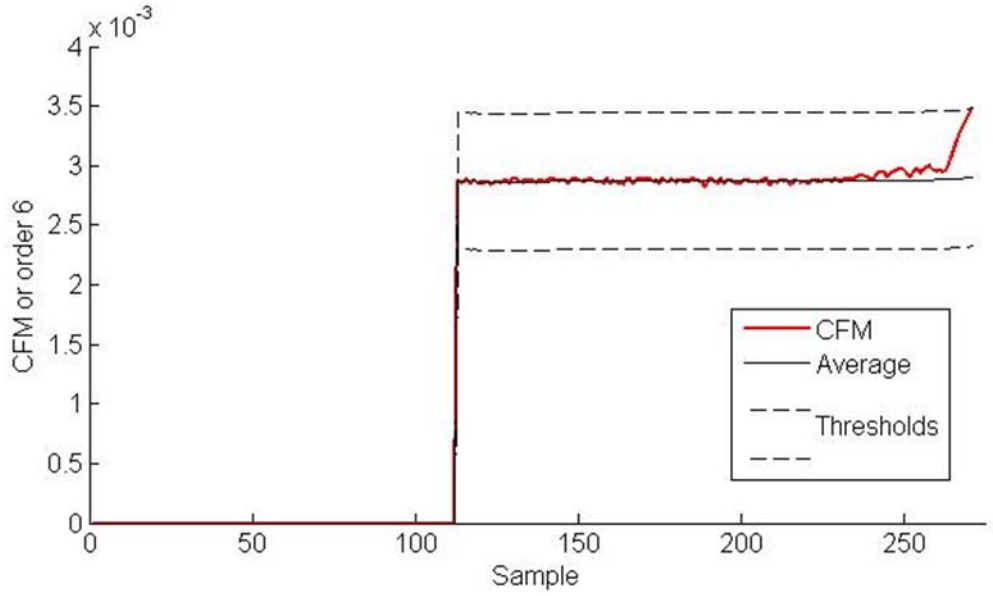

Figure 5.8 Chebyshev Focus Measure calculated in Phase 5 and the corresponding threshold levels

only calculated during the last phase of the attachment step, when the particle is being brought down. The threshold limits have also been plotted. The automated stage stops as soon as the CFM of the tip region crosses one of the two bands. In this particular case, the AFMC was not in focus initially. Hence when it bends it first comes in focus, thus providing the final spike before the process is triggered off.

An image of the multi-axis AFMC created is shown in Fig. 5.9. The sampling frequency was 15 Hz. Thus the process was completed within 20 seconds.

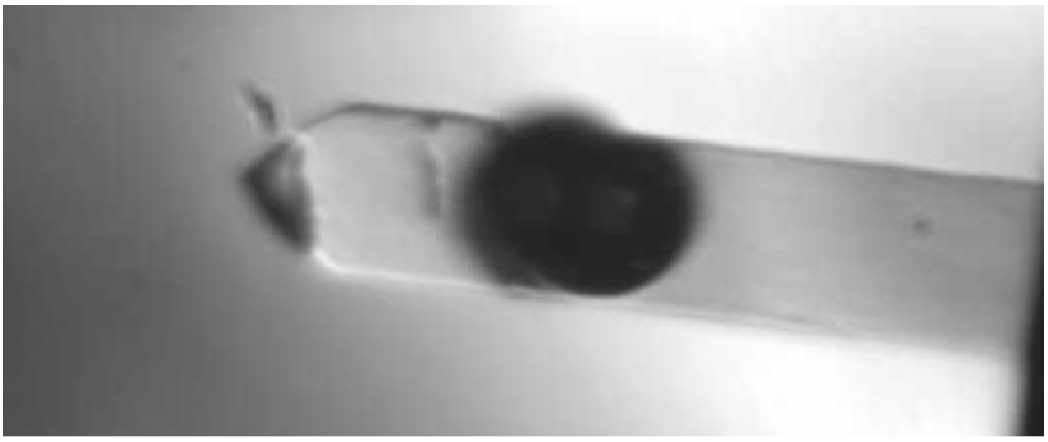

Figure 5.9 Image of AFMC with the particle attached

5.4 Summary

The results from different steps of the automated stage were presented in this chapter. The performance of the process was described with respect to different system parameters. Only the particle attachment results have been described, as the other steps use similar control framework and produce similar performances.

CHAPTER 6

SUMMARY AND FUTURE WORK

6.1 Summary

Fabrication of a multi-axis AFMC from a traditional AFMC involves attaching a magnetic particle close to the end, among other steps. It was conventionally done manually, causing considerable stress to the users. The requirement of no unnecessary body movement is very hard to repeat every single time. The consequences of inability to do so include damage to the AFMC in some circumstances and a lot of frustration otherwise. This work developed an automated process to replace the key manual tasks during the magnetic particle attachment process. It relied on visual feedback.

A setup was designed to observe this process and capture it using a Hitachi CCD camera. The images were processed using the algorithms developed to extract the location information of the objects to be manipulated. As multiple steps have been automated, each step requires manipulation of a different object. This was done using only one image unlike the stereovision. A control strategy was developed to actuate Nanocube, a piezo stage using the feedback from the camera. It was based on an image

formation model that was derived to relate a three-dimensional point to its image location.

The image processing algorithms were designed to be robust against different parameters like noise, change in illumination intensity, illumination pattern, different size of the objects required to be manipulated and dust in the optical path of the microscope. Some key features from each object were used to aid their detection and tracking.

System parameters required during the automated process were calibrated. Algorithms were designed to calibrate others which change from experiment-to-experiment. A vibration rejection scheme was developed to reduce the error in the calibration process.

The control process was implemented in various steps of the entire particle attachment process. Its performance was demonstrated by attaching a particle to an AFMC. The designed process was shown to be much faster. In fact it took only 20 seconds to complete the final attachment step. Its robustness was proven by running it under varying conditions and different user requirements.

6.2 Future Work

The main constraint of this process is due to the hardware used. Because of the low motion range of the piezo-actuator, the process has been only partly automated. The process can be completely automated by using proper hardware in the future.

BIBLIOGRAPHY

[1] G. R. Jayanth, Sissy M. Jhiang, and Chia-Hsiang Menq. Two-axis probing system for atomic force microscopy. *Review of Scientific Instruments*, 2008.

[2] See www.afmuniversity.org/chapter7.html for applications of the AFM in different fields.

[3] J. K. H. Hörber and M. J. Miles. Scanning Probe Evolution in Biology. *Science*, 2003.

[4] B. Bhushan, J. N. Israelachvili, and U. Landman. Nanotribology: friction, wear and lubrication at the atomic scale. *Nature (London)*, 2003.

[5] J. E. Griffith, D. A. Grigg, M. J. Vasile, P. E. Russell, and E. A. Fitzgerald. Scanning probe tip geometry optimized for metrology by focused ion beam ion milling. *Journal of Vacuum Science and Technology B*, 1992.

[6] Y. Martin, F. Zenhausern, H.K. Wickramasinghe. "Scattering Spectroscopy of Molecules at Nanometer Resolution". *Applied Physics Letters*, 1996.

[7] Felix Krahmer, Youzuo Lin, Bonnie McAdoo, Katharine Ott, Jiakou Wang and David Widemannk. Blind Image Deconvolution: Motion Blur Estimation. August 18, 2006.

[8] P.T. Yap and P. Raveendran. Image focus measure based on Chebyshev moments. *IEE Proceedings in Vision, Image and Signal Processing*, 2004.

[9] W.T. Ang**,** F.A. Garmbn, P.K. Khosla, and C. N. Riviere. Modeling Rate-dependent Hysteresis in Piezoelectric Actuators. *Proceedings of the IEEE/RSJ International Conference on Intelligent Robots and Systems*, 2003.

[10] H.C. Lee. Review of image-blur models in a photographic system using the principles of optics. *Optical Engineering*, 1990